# SCIENTIFIC RESEARCH AND EVALUATIONS 2024

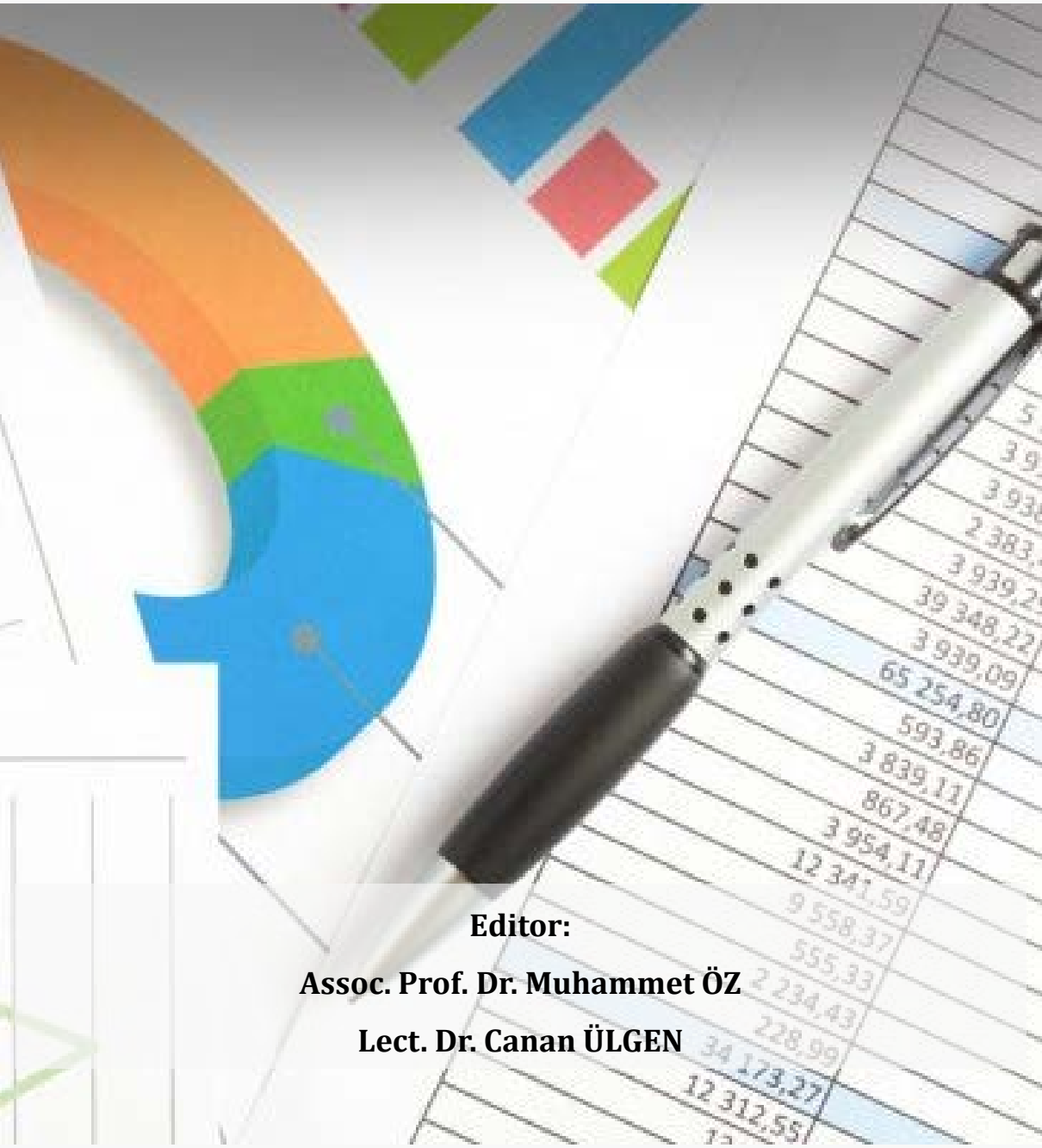

**Editor:**

**Assoc. Prof. Dr. Muhammet ÖZ**

**Lect. Dr. Canan ÜLGEN**

yaz

yayınları

# SCIENTIFIC RESEARCH AND EVALUATIONS 2024

*Editors*

**Assoc. Prof. Dr. Muhammet ÖZ**

**Lect. Dr. Canan ÜLGEN**

yaz yayınları

**2024**

yaz yayınları

# SCIENTIFIC RESEARCH AND EVALUATIONS 2024

Editor: Assoc. Prof. Dr. Muhammet ÖZ

ORCID NO: 0000-0003-0049-0161

Editor: Lect. Dr. Canan ÜLGEN

ORCID NO: 0000-0002-8272-3370



E_ISBN 978-625-6171-19-0

Aralık 2024 – Afyonkarahisar

Dizgi/Mizanpaj: YAZ Yayınları

Kapak Tasarım: YAZ Yayınları

YAZ Yayınları. Yayıncı Sertifika No: 73086

M.İhtisas OSB Mah. 4A Cad. No:3/3
İscehisar/AFYONKARAHİSAR

www.yazyayinlari.com

yazyayinlari@gmail.com

info@yazyayinlari.com

**CONTENTS**

# IN VITRO TESTING OF THE BIOCOMPATIBILITY OF MEDICAL DEVICES

**Busra MORAN BOZER**[1]

## 1. INTRODUCTION

In the rapidly developing world, many disciplines are coming together to develop new medicines and products to diagnose, treat and enhance the patient's comfort zone. Medical devices are products that include many simple and/or complex products designed to diagnose, treat and enhance the patient's comfort zone (Leveson, 1995). Researchers and manufacturers around the world are aware that newly developed and emerging drugs and devices undergo many tests during and after the development phase before they are put into use. Although the tests to be performed vary according to the intended use and location, it is extremely important to know the purpose of these tests, to interpret them correctly and to follow the test sequence in order to manage both the quality of the product and the time and cost to the manufacturer (Bronzino, 2006). This section of the book provides detailed information on the purposes and details of in vitro biocompatibility tests that should be performed on medical

[1] Dr. Hitit University, Scientific Technical Research and Application Center,In Vitro Biocompatibility Laboratory, busra.moran@gmail.com , ORCID: 0000-0002-7280-4417

devices. This will assist researchers who are conducting or planning to conduct their studies in this way.

## 2. CONCEPT AND SCOPE OF THE MEDICAL DEVICE

If it is desired to define the medical device, it is not possible to express it in one clear sentence. This is because medical devices and medicinal products for the treatment of diseases do not belong to the same category and should not be confused. Medical device according to EU standards; During its use, it does not perform its primary function by pharmacological, immunological or metabolic action, but may be assisted in the performance of its function by such action, and is intended to be used for the diagnosis, prevention, monitoring, treatment, alleviation of disease and/or disability in human beings, or for investigational purposes, All types of tools, instruments, equipment, software, accessories or other materials, including software, capable of being used alone or in combination, which are specifically designed by the manufacturer for diagnostic and/or therapeutic purposes and which are necessary for the medical device to perform its intended function" (Resmi Gazette 2011).

The wide range of medical devices makes it difficult to classify them, but if a general classification is desired, 15 classes of medical devices can be mentioned (ranging from medical imaging systems to disposable consumables). Testing, acceptance criteria and use of medical devices are based on 3 basic disciplines in the world. America, China and the countries of the European Union have established

their legislation and certify products under this legislation. Turkey and many non-EU countries are also subject to EU legislation in the production and certification of medical devices. The design, certification, production, registration, placing on the market and use of medical devices is the history of a medical device. In the design and certification part, the requirements and tests for medical devices play an important role.

### 2.1. Classification Of Medical Devices

Medical devices are basically divided into five classes according to their use, location and nature (Table 2.1). Depending on the class, there are a number of necessary and mandatory tests.

**Table 2.1: Classification of Medical Devices**

| Class | Type of Medical Device | Example |
|---|---|---|
| Class I | Devices that generally do not come into contact with the organism. Low risk for the patient. | Body fluids collection devices (blood, urine, etc.), such as measuring device electrodes. |
| Class IIA | The risk for the patient is moderate. Contact with the organism is not direct but interventional. Their administration is through natural body cavities (veins, muscles, etc.). They cannot remain in the body after administration. Including those used in diagnostics and wound healing. | Catheters, syringes, blood tranfusion devices, drug-free tapes, bandages, etc. |
| Class IIB | The risk for the patient is moderate. They are devices that can be partially and/or completely implanted into the organism. They can modify the physiological composition of body fluids. | Medicated bandages, such as dialysis apparatus |
| Class III | They may pose a high risk to the patient. They are generally used in cases where vital organs cannot fulfil their function. They provide life support. | As well as fibrillators, knee, spine etc. implants, breast implants, prostheses. |

Chemical and physical characterisation tests are the main tests performed by the manufacturer when developing a product for a specific purpose (Wang et al., 2022). These tests are followed by pre-clinical and clinical studies depending on the intended use in humans. Tests that should be carried out in in vitro environments prior to clinical studies, in vitro biocompatibility tests, followed by animal tests if necessary, and tests carried out on tissues produced in the laboratory environment without the use of experimental animals, which have recently been accepted for cosmetic products and are expected to replace them in other products (Albert, 2022). The table of mandatory biocompatibility tests to be performed according to their class is given in Table 2.2 according to FDA and EU standards. The biocompatibility tests for medical devices in the EU Directives are evaluated within the scope of EN ISO 10993. Table 1.2 has been prepared in accordance with EN ISO 10993:1. The tests used to assess the biocompatibility of devices are considered in two parts: in vitro and in vivo. In vitro tests are tests on cells obtained from living organisms in a laboratory environment, while in vivo studies are tests on experimental animals (rat, mouse, rabbit, etc.). In the context of ethical values, in vitro studies are a must before in vivo studies. Animal welfare, budget, experienced personnel and evaluation of results are extremely important in experimental animal testing. This book chapter provides information on in vitro biocompatibility testing, logic and interpretation.

**Table 2.2: Biocompatibility test matrix (EN ISO 10993:1)**

| Product Category | | | Biological Effects | | | | | | | | | | | |
|---|---|---|---|---|---|---|---|---|---|---|---|---|---|---|
| Body contact | | Contact Duration | Cytotoxicity | Sensitisation | Irritation/intra-skin | Acute systemic toxicity | Subchronic toxicity | Genotoxicity | Implantation | Blood compatibility | Chronic toxicity | Carcinogenicity | Reproductive/developmental | Biodegradation |
| Surface Devices | Skin | A | x | x | x | | | | | | | | | |
| | | B | x | x | x | | | | | | | | | |
| | | C | x | x | x | | | | | | | | | |
| | Mucosal wall | A | x | x | x | | | | | | | | | |
| | | B | x | x | x | o | o | | o | | | | | |
| | | C | x | x | x | o | x | x | o | | o | | | |
| | Treacherous | A | x | x | x | o | | | | | | | | |
| | | B | x | x | x | o | o | | o | | | | | |
| | | C | x | x | x | o | x | x | o | | o | | | |
| Surfaces with External Contact | Blood pathway | A | x | x | x | x | | | | x | | | | |
| | | B | x | x | x | x | o | | | x | | | | |
| | | C | x | x | o | x | x | x | o | x | o | o | | |
| | Tissue/Bone | A | x | x | x | o | | | | | | | | |
| | | B | x | x | x | x | x | x | x | | | | | |
| | | C | x | x | x | x | x | x | x | | o | o | | |
| | Blood Circulation | A | x | x | x | x | | o | | x | | | | |
| | | B | x | x | x | x | x | x | x | x | | | | |
| | | C | x | x | x | x | x | x | x | x | o | o | | |
| Implants | Tissue/Bone | A | x | x | x | o | | | | | | | | |
| | | B | x | x | x | x | x | x | x | | | | | |
| | | C | x | x | x | x | x | x | x | | o | o | | |
| | Blood | A | x | x | x | x | x | | x | x | | | | |
| | | B | x | x | x | x | x | x | x | x | | | | |
| | | C | x | x | x | x | x | x | x | x | o | o | | |

Contact duriation A: limited (<24h), B: prolonged (24h-30 day), C: permaned (>30 day)

x= Tests specified in ISO 10993-1 standard

o= Tests required for application to the American (FDA) market

## 3. IN VITRO BIOCOMPATIBILITY TESTS

Before going into the details of these tests, it is necessary to mention the term biocompatibility. Biocompatibility is the ability of materials to respond appropriately to the body system during human use, to be compatible with the body, without interfering with the function of the surrounding tissues and without causing inflammation (Güven, 2014). It is the optimal compatibility of the biomaterial or medical device with the body. Biocompatibility testing is performed in both in vitro and in vivo environments to demonstrate the suitability of the developed materials for use in living organisms and, in cases where clinical research is required, to minimize the negative consequences that may occur in clinical research.

The first step in medical device development begins with the selection of the material to be used. It should be chemically and physically suitable for the intended use. For example, a new medical device made from a material that has been shown to be toxic in the literature and in the clinic will not pass the relevant tests anyway, resulting in a waste of time and budget. For this reason, it is extremely important that the raw materials of the selected materials comply with the standards and are safe for human health. The most commonly used test method for in vitro biocompatibility of the developed medical device is the cytotoxicity method. This is followed by genotoxicity and blood interaction tests. 3D tissues used in in vitro biocompatibility are also a continuation of these tests.

### 3.1. Cytotoxicity Tests

When assessing the biocompatibility of medical devices, the EN ISO 10993 series of tests are accepted in EU Directives. Each series of the standard describes different test methods in detail and provides test procedures. For cytotoxicity methods, EN ISO 10993: 5 "Biological evaluation of medical devices - Part 5: In vitro cytotoxicity tests" is used as a reference. Cytotoxicity is a method of testing the toxic effects of substances or materials on cells (Horvath, 1980). In this method, numerical values are obtained by calculations based on the response of cells to the applied substance and cell viability, and interpretation is made for the in vitro cytotoxicity of the substance (Mossman, 1983). There are many academic methods for cytotoxicity testing. According to EN ISO 10993:5, it is sufficient to select one of the 5 different cytotoxicity methods suitable for the material. The MTT (3-(4,5-dimethylthiazol-2-yl)-2,5-diphenyl tetrazolium bromide), XTT and Neurtal red methods are the most commonly used. In this section, the most commonly used MTT method is mentioned.

#### 3.1.1. Determination Of Cytotoxicity Using The MTT Method

The MTT method is completed by reading the absorbance of formazan crystals formed in living cells after dissolution with the appropriate solvent in a multiplex reader. This method is used for many researches; drug development, cellular pathways, evaluation of biomaterials, etc. If it is necessary to follow the method from the beginning, the steps to follow are given below.

#### 3.1.1.1. Cell Culture

Cell culture is an environment where different tests are carried out by many researchers, which forms the basis of studies in many interdisciplinary fields, cost, time saving, fast results, open to modification. In the evaluation of medical devices, healthy cells in cell culture are preferred and interpretation is based on the response of these cells. The most ideal condition for storing cells without losing their functions is the environment of -196 $^{o}$C liquid nitrogen. The first step is to remove the cells from the freezing environment and thaw them before the tests to be performed. Once the cells have been removed from the freezing medium, they are immediately centrifuged out of the freezing liquid and brought together with the medium in which they can proliferate (Erdem et al., 2021). All these procedures are carried out in laminar class II cabinets, in a sterile environment and with sterile materials. Passaging at least twice is very important for the stability of the response to the products, allowing the cells to proliferate and adapt to the flasks in the cabinet. The following steps are taken to open and culture the donated cells;

- Cells are removed from -196$^{o}$C, cryotubes are rapidly thawed in a 37$^{o}$C water bath.
- In a laminar class II cabinet (the cabinet should be cleaned before and after each use), place in a sterile falcon tube.
- Add medium from the cells used to the volume of liquid transferred to the Falcon tubes.
- Centrifuge for 2 minutes at 2000-2500 rpm.

- Treat the resulting pellet with the appropriate medium for the cell line being studied and mix gently.
- Transfer the cells to appropriate flasks according to the amount of pellet and incubate at 37°C in an incubator containing 5% CO2 and humidity. The medium is changed every 48 hours according to the proliferation status of the cells.
- When the cells cover the bottom of the flask, the cells are removed with trypsin enzyme and the cells are passaged into new flasks.
- The same procedure is repeated until the number of cells to be used is reached.

Points to note at this stage: the natural division and proliferation cycle of cells is between 22-24 hours (may vary according to cell type), if the passaging process to be performed after the completion of this cycle, there will be no major deviations between the responses to the substances applied to the cells. The MTT protocol begins after this stage. Plates with 96 wells are preferred for MTT studies. The steps are as follows

- Cells are transferred to plates with 10,000 cells per well.
- It is important to have at least 4 replicates for each substance to be applied.
- The cells are incubated for 24 hours to allow them to adhere to the plates.

- After 24 hours of incubation, the medium is removed from the environment and the extraction fluids in which the substances are prepared are applied to the plates.
- According to the standard, 24 hours exposure is optimal. Cells are treated with substance liquids for 24 hours. For the control group, only medium is applied without any application to the cells.
- After 24 hours of interaction with the substance, the medium is removed and the prepared MTT solution is added to the cell medium (MTT solution is prepared at 5mg/ml in academic studies and dissolved with DMSO, while it is recommended to dissolve at 1mg/ml concentration in the standard and dissolve with isopropyl alcohol).
- After 2.5-3 hours of MTT treatment, double the amount of solvent of the MTT solution is added to the MTT treated cells and the formosan crystals formed are dissolved.
- The solvent, which is kept for a maximum of 15 minutes, is shaken well and the absorbance is measured at a wavelength of 570 nm.
- The absorbance value obtained from the negative control value is considered as 100% viability and is divided by the absorbance value obtained from the treated wells.

Interpretation: The viability value obtained is expressed as a percentage. Viability values below 70% are considered in vitro biocompatible according to EN ISO

10993, while results above 70% are considered in vitro biocompatible. If the result is in vitro biocompatible but the material is expected to be biocompatible, the test is repeated and considered as such if the result has not changed. However, if the result has changed, the test is repeated a third time and evaluated according to the average of the three results (Dogan et al., 2023).

For medical devices with short-term contact, the extraction time of the material can be changed and reported as such. For medical devices with long-term contact, even if the 24-hour result is biocompatible, it is recommended to apply 48 and/or 72 hours in cellular interaction for compatibility of further tests.

### 3.2. Genotoxicity tests

Genotoxicity tests are described in detail in EN ISO 10993:3. The purpose of this test is to determine the breakdown of parts that cause damage to the genetic material in the cell. Although not all genotoxic substances are mutagens, all mutagens have genotoxic effects. Genotoxic substances are the most damaging and cause cancer. Another important point is that some genotoxic substances alter the genetic information leading to mutogenicity. There are different distributions for this test, which is particularly important for medical devices that are intended to remain in the body. Although the standard does not specify the methods of these tests, it recommends the OECD installation standards. Accepted OECD standards; 471 and 473 direction.

There are two genotoxicity methods that can be used in the cell, the first is the chromosome aberration test and

the second is the micronucleus genotoxicity test. The method to be chosen is determined by the medical device. This section describes the micronucleus genotoxicity test that is commonly used for in vitro genotoxicity testing.

### 3.2.1. Determination Of Genotoxicity By The Micronucleus Method

The cell culture method described in section 3.1.1.1 is used in this test. The cell line used varies in this test method. Epithelial cells are preferred for this test method. The most commonly used cell line is CHO (Chinese hamster ovary). 12 or 6-well plates are used, which are multiplied by the classical cell culture method. After completion of the adaptation phase of the cells, the experimental system for the 12-well plate is given below (Elen et al., 2023).

- It is evenly distributed, with 100 000 cells in each well. It is incubated for 24 hours.
- After incubation, the human body is dressed and the collected material extract is applied.
- 44-48 days after the 24-hour incubation, the plate is collected. At the same time, the human aggregate is removed and the division phase is stopped with Cyt-B (cytochalasin B block) solution. This is the most important step in the test. Breaks in the cells, which are divided into poles and have two nuclei within the same cell membrane, are identified by staining with dyes.
- After incubation, the cells are stained with a fluorescence-labelled dye (e.g. PI, propidium iodide)

or a dye that can be observed under a light microscope (e.g. Giemsa). The cells are fixed with fixative and mounted with the appropriate microscope onto the labelled dye.

- Continue counting after the transaction has been published. A total of at least 2000 cells should be counted. Cells are counted as binucleated, multinucleated, mononucleated and micronucleated.
- A known genotoxic material is used as a positive control.

Interpretation: The ratio of the total of the two nuclear intervals of the micronucleated part is important. In addition, the CBPI (cytokinesis block proliferation index), RI (replication index) and MI (mitotic index) values were determined in the ratios obtained. It is important that these values are tested and their reliability determined. While cells disintegrate when exposed to any external attack, micronucleated cells can only be observed at a rate of approximately 5-10 micronucleated cells per 2000 cells. The increase in this ratio is used and interpreted for the genotoxicity of the material.

### 3.3. Blood Interaction Testing

If biomaterials and medical devices used in vascular access, or the medical device to be used, have any interaction with blood, it is necessary to perform blood interaction tests according to EN ISO 10993. Blood interaction tests are detailed in EN ISO 10993:4 and the standard explains these test methods according to the

purpose of the medical device to be used. Blood interaction tests performed in vitro; they are generally grouped into aggregation, haemolysis and coagulation factor tests. The most commonly used in vitro test is the haemolysis test.

### 3.3.1. Determination Of In Vitro Haemolysis

EN ISO 10993:4 refers to the ASTM F756 standard as the reference for determining the haemolytic effect (Gürler and Moran, 2022). The steps in this test are as follows.

- Certified rabbits are used in this test. The haemolytic values of blood collected from 3 different donors are determined and the value of the blood to be tested is required to be 10±1.
- Blood is collected in an EDTA tube and gently shaken to prevent clotting.
- Determine the haemoglobin concentration using the Drabkin haemoglobin assay.
- It is necessary to construct a calibration curve. Prepare dilutions between 0.02-0.8 mg/mL according to the standard using the prepared haemoglobin calibrator. Read the prepared dilutions at 540 nm and obtain the calibration coefficient (F).

Plasma Free Haemoglobin (PFH) is calculated from the collected blood and its values are determined;

- Blood from three donors is mixed and 3.0 mL of the blood is centrifuged for 15 minutes at 700-800 G in a standard clinical centrifuge.

- After centrifugation, dilute the plasma 1:1 with cyanmethaemoglobin reagent, Drabkins solution or other approved diluent. (e.g. 0.5 mL plasma is added to 0.5 mL cyanmethaemoglobin reagent).
- After 15 minutes, read the absorbance at 540 nm. The plasma haemoglobin ratio is calculated from the F value obtained from the standard curve. Plasma free haemoglobin (mg/ml) is calculated as follows
- Plasma Free Haemoglobin (PSH) = A PSH x F x 2
- If PSH is less than 2 mg/mL, continue the test. If the PSH is 2mg/ml or more, this sample should be discarded and another blood sample taken.

The second step is to determine the total blood haemoglobin concentration;

- Add 20 µL of a well-mixed pooled whole blood sample to 5.0 mL of cyanmethaemoglobin, Drabkin's solution or other approved diluent.
- Allow the resulting solution to stand for 15 minutes for Drabkin's solution or 5 minutes for cyanmethaemoglobin reagent and then read the absorbance of the solution using a spectrophotometer at a wavelength of 540 nm.
- The total haemoglobin concentration is calculated from the absorbance values obtained, the F value obtained from the haemoglobin concentration and the dilution factor of the blood: Total blood haemoglobin concentration (C) = A C x F x 251. The result obtained should be 10 ± 1. If the result is not

within the desired range, the whole blood is diluted with PBS without calcium and magnesium, mixed again with Drabkin's solution and left for 15 minutes at room temperature, then the absorbance at 540 nm is read.

- The haemoglobin concentration extracted from the blood (1 mL) is added to the test material (7 mL).
- The tubes are kept in a suitable test tube rack in a water bath or oven at 37 ± 2 °C for at least 3 hours. At the end of the incubation period, the liquid is transferred to a suitable tube or centrifuged with the same tubes in a standard clinical centrifuge at 700-800 G for 15 minutes.
- Carefully remove the supernatant and transfer to a second screw-capped tube. Note the presence of any colour in the supernatant and its clarity or turbidity.

The haemoglobin concentration of the supernatant is determined by the following method.

- Add 1 mL of supernatant to 1 mL of cyanmethaemoglobin or Drabkin's reagent. Prepare negative, positive and blank controls separately for each test item. Allow the samples to stand at room temperature for 15 minutes for Drabkin's reagent or 3 to 5 minutes for cyanmethaemoglobin reagent. Read the absorbance of the solution on a spectrophotometer at a wavelength of 540 nm.

Calculate the haemoglobin concentration in each supernatant from the calibration curve.

- The haemoglobin concentration of the supernatant from the test sample or control tubes is calculated as follows
- S = AS x F x 2 (S: haemoglobin concentration of the supernatant; AS: absorbance of the supernatant; F: calibration curve).
- The haemoglobin concentration of the blank is calculated as follows
- B = AB x F x 2 (B: blank haemoglobin concentration; AB: absorbance of the supernatant; F: calibration curve)
- % haemolysis (haemolytic index) is calculated as follows:
    - % haemolysis = (supernatant haemoglobin concentration x 100%) / total haemoglobin concentration

Interpretation: If the % haemolysis value obtained is between 0-2% it is reported as having no haemolytic effect, if it is between 2-5% it is reported as mildly haemolytic and if it is greater than 5% it is reported as having a haemolytic effect. However, a visual clarity test should also be evaluated.

This method uses the haemolytic potential of medical devices in comparison to a negative control material generally considered suitable for blood contact applications. Materials with a higher haemolytic potential

than the negative control material, which are known to have excellent performance in blood contact situations, should be carefully considered for use as they may or may not be a potential cause of haemolysis in vivo. It should not be claimed to be the most sensitive or specific method for assessing the haemolytic potential of all materials in all applications. The results obtained with this method are intended to be used in conjunction with the results of other tests in evaluating the blood compatibility of the test material (Bozer et al., 2023).

## 4. CONCLUSION

The first step in the design and manufacture of a medical device should be to determine the purpose for which the product will be used. Once the purpose has been determined, every step must be taken with care and attention, starting with the initial design of the products. Testing in a laboratory environment before use on humans minimises problems that may arise in the future (Albert 2002). The values and equipment determined for chemical characterisation tests carried out in vitro are explained in detail in the standards and are not subject to interpretation, except in specific cases. However, it is extremely important to increase the quality and safety of the product through in vitro biocompatibility testing. Reproducing a cytotoxic material in a way that eliminates its effects prevents future financial losses (Jones et al., 2022). A material with a cytotoxic effect may not show a cytotoxic effect when used with the appropriate method (according to its intended use). The main logic of the genotoxicity test method is

given. S9 (liver growth factor) is used in the test and the procedure takes quite a long time. For this reason, the method is briefly mentioned in order to understand the main logic. For this reason, the expertise, interpretation skills and literature knowledge of the testing personnel can support product development. The test methods given in this section are given superficially to understand the main logic. In order for the methods to be applied directly, reference standards must be provided and carried out in that way. By bringing all these purposes and reasons together, less cost and time loss can easily be avoided in the development of new products. These tests should be given importance to avoid problems in product certification and to help the patient.

**REFERENCES**

7. T.C. Resmi Gazette (2011) Regulation on Active Implantable Medical Devices. 27957, 07.06.2011.

Albert, D. E. (2002). The growing importance of materials characterization in biocompatibility testing. *Medical Device and Diagnostic Industry*, *24*(3), 50-59.

Bozer, B. M., Özkahraman, B., & Mert, H. (2023). Photocrosslinked methacrylated pectin and methacrylated hyaluronic acıd wound dressing loaded with oleuropein as bioactive agent. *International Journal of Polymeric Materials and Polymeric Biomaterials*, 1-13.

Bronzino, J. D. (Ed.). (2006). *Medical devices and systems*. CRC press.

Dogan, D., Erdem, U., Bozer, B. M., Turkoz, M. B., Yıldırım, G., & Metin, A. U. (2023). Resorbable membrane design: In vitro characterization of silver doped-hydroxyapatite-reinforced XG/PEI semi-IPN composite. *Journal of the Mechanical Behavior of Biomedical Materials*, *142*, 105887.

Elen, L., Turen, Y., Cicek, B., Bozer, B. M., Saud, A. N., & Koc, E. (2023). The cytotoxic and genotoxic assays of Mg-Ag Alloy doped with Zn, Ca, and Nd elements. *Journal of Materials Engineering and Performance*, *32*(16), 7337-7347.

Erdem, U., Bozer, B. M., Turkoz, M. B., Metin, A. U., Yıldırım, G., Turk, M., & Nezir, S. (2021). Spectral analysis and biological activity assessment of silver

doped hydroxyapatite. *Journal of Asian Ceramic Societies*, *9*(4), 1524-1545.

Gürler, M., & Bozer, B. M. (2022). A new era in fundamentals of bone homeostasis: biocompatibility of bone mineral doped fluoride ions with osteoblast cells in the balance of calcium and phosphate metabolism. *Anatolian Current Medical Journal*, *4*(3), 265-272.

Güven, Ş. (2014). Biyouyumluluk ve biyomalzemelerin seçimi. Mühendislik Bilimleri ve Tasarım Dergisi, 2(3), 303-311.

Horvath, S. (1980). Cytotoxicity of drugs and diverse chemical agents to cell cultures. Toxicology, 16(1), 59-66

Jones, D. S., Lorimer, C. P., McCoy, C. P., & Gorman, S. P. (2008). Characterization of the physicochemical, antimicrobial, and drug release properties of thermoresponsive hydrogel copolymers designed for medical device applications. *Journal of Biomedical Materials Research Part B: Applied Biomaterials: An Official Journal of The Society for Biomaterials, The Japanese Society for Biomaterials, and The Australian Society for Biomaterials and the Korean Society for Biomaterials*, *85*(2), 417-426.

Leveson, N. (1995). Medical devices: The therac-25. *Appendix of: Safeware: System Safety and Computers*.

Mosmann, T. (1983). Rapid colorimetric assay for cellular growth and survival: application to proliferation

and cytotoxicity assays. Journal of immunological methods, 65(1-2), 55-63.

Wang, H., Yu, H., Tran, T. N., Fu, K., Kiley, K., Kullar, S., ... & Kamberi, M. (2022). Chemical Characterization of Leachables in Catheter Device. *ACS omega*, *7*(51), 48291-48300.

# PERFORMANCE PARAMETERS OF SOLAR ENERGY SYSTEMS IN PANEL TECHNOLOGIES AND THEIR EFFECTS IN PRACTICE

**Muhammed Said ULAŞ**[1]

**Ahmet TURŞUCU**[2]

## 1. INTRODUCTION

There are many types of energy on earth in terms of kinetic and potential. These energies are released through different ways, substances, and methods such as mechanical, chemical, thermal, magnetic, light, and electrical energy. Electrical energy is taking more and more place in our lives every passing day, and we are in a position where we cannot even think of a moment without energy. In the periods when electricity was not widely used in every field except lighting, the efficiency and energy losses of the materials produced for consumption were high. This inefficiency and loss affected the installed power of the energy to be produced according to the supply-demand balance. As a result of research and development (R&D) studies carried out on almost all materials that consume electricity over time, efficiency has increased.

[1] M. Sc., Graduate School of Education, Şırnak University, muhammedsaidulas07@gmail.com.

[2] Electrical and Electronics Engineering, Sirnak University, Sirnak, Türkiye

Losses have been tried to be reduced to minimum levels, and this situation continues. Due to the increase in the number of consumers and the areas of use of electrical energy, the installed power of the required energy has also increased over time.

Unfortunately, there is still a large share of the use of resources that harm the ecosystem in order to meet the increasing energy demand. Apart from these resources, there are many resources used within the framework of the search for environmentally friendly energy, and the low performance of electricity produced from solar energy, one of the resources included, has led to many research studies on this subject (Tunçkaşık & Köse, 2022). Electricity production from solar energy is done by photovoltaic cells (also called solar cells and solar cells) containing semiconductor material and the panels formed by these cells. Semiconductor materials such as silicon (Si), cadmium telluride (CdTe), gallium arsenic (GaAs), and copper indium diselenide (CuInSe2) are used in solar cells. Photovoltaic cells directly convert the energy they receive from the sun without any intermediaries such as generators (Istanbul Technical University, 2023).

Silicon is the most commonly used semiconductor material. There are sand and quartz types. After passing through many stages and gaining its pure feature, polycrystalline or single-crystalline silicon is made.

## 2. HISTORY OF PHOTOVOLTAIC CELLS

A French physicist named Edmond Becquerel first observed in 1939 that voltage was generated between electrodes placed in a conductive liquid by light falling on the liquid. This situation is defined as the beginning of the photovoltaic phenomenon. In 1876, R. Day and G. Adams tried this phenomenon for the first time in solids on selenium crystals.

In the early days, research and development activities carried out at the higher education level later created a great resonance among the public regarding renewable energy in terms of environmental sensitivity, and large institutions assumed responsibility for solar energy production. With the developing technology and increasing demand for energy, these large institutions increased the production of photovoltaic cells, causing costs to decrease (Istanbul Technical University, 2023).

## 3. SOLAR CELLS AND THEIR WORKING PRINCIPLE

Solar cells made of semiconductor materials use the visible light spectrum to produce energy. Although weathering in the atmosphere blocks most of the visible light, the entire spectrum is not eliminated. An example cell is shown in Figure 3.1.

**Figure 3.1. Solar Cell ('Antalya Energy', 2023).**

### 3.1. Semiconductor Materials Used in Cells

The electrical effect is related to the band properties in materials. As seen in Figure 3.2, if the bands are full or empty in terms of energy, the material is an insulator. In other materials (conductors and semiconductors), there is space for electrons to move.

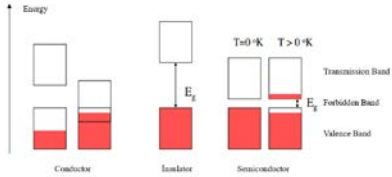


**Figure 3.2. Conductor, Semiconductor and Insulator Band Gaps. (Electronic Properties of Semiconductors, 2023)**

Apart from the original semiconductors, there are also n-type -p-type doped semiconductors used in solar cells, depending on the bond structure they create. When the phosphate (P) element forms a bond with silicon, the electron density in the crystal increases; materials that show this property are called n-type semiconductors, as seen in Figure 3.3. The boron (B) element takes electrons from the crystal in the bond it makes with silicon. In this case, the buoyant density of the material increases. Materials that show such a property are p-type semiconductors.

In Figure 3.3, Ef is the Fermi Level, Ed is the Donor Energy Level, and Ea is the Acceptor Energy Level (Electronic Properties of Semiconductors, 2023).

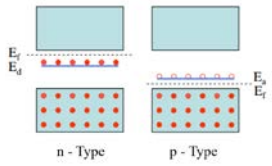


**Figure 3.3. Doped Semiconductor Representations (Electronic Properties of Semiconductors, 2023).**

There are some reasons for using semiconductor materials instead of conductors in solar cells. The electrons that roam freely in conductors, along with this circulation, do not have a forbidden band gap in conductor atoms, as seen in Figure 3.2. For this reason, it responds quickly to the light coming from the sun and reflects the light. Since there is no separate energy layer where the electrons in the substance can separate from the positive holes and settle as a result of the response it receives from the light, no electrical energy is produced through radiation.

As seen in Figure 3.4, in semiconductors, the valence band (full valence) and the conduction band are separate from each other and contain a forbidden band that does not allow electrons to pass between them. When the width of the forbidden band gap increases, the conductivity decreases or becomes insulating.

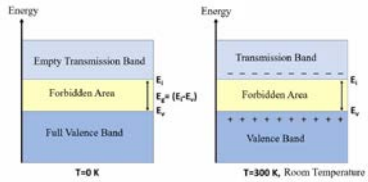


**Figure 3.4. Thermally Triggered Semiconductor Demonstration (Ankara University, 2023)**

In some semiconductor materials, the band gap value is the same as 2.5 eV. It cannot always be compatible with the solar radiation spectrum, and therefore, this type of material is not preferred due to the decrease in efficiency. The ideal and average efficiency rates of semiconductors seen in Figure 3.5 and Figure 3.6 are the most suitable efficiency that responds to both wide range and photovoltaic conversion when the photon energy reflected from the sun (taking into account the color spectrum) is in the range of 1 eV - 2 eV (Istanbul Technical University, 2023).

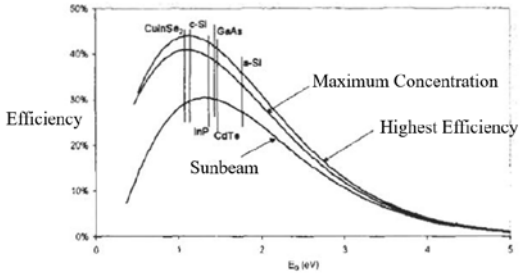


**Figure 3.5. Efficiency Ratios of Some Semiconductors According to Energy Band Gaps (Istanbul Technical University, 2023).**

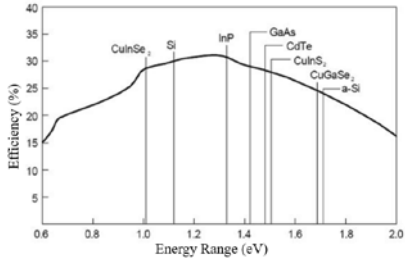


**Figure 3.6. Average Efficiencies of Some Semiconductors According to Energy Range (Istanbul Technical University, 2023).**

There are colors from blue to red in the light spectrum reflected in the solar cell. As the color approaches red, the photon energy shows a decreased curve from high to low. As seen in Figure 3.7, the energy of the photon is transferred to the valence band by the reflection of light in the cell, and the number of electrons increases. The increased electron passes through the forbidden band in the semiconductor and passes to the conduction band. However, it leaves a positive space charge in its place (Istanbul Technical University, 2023).

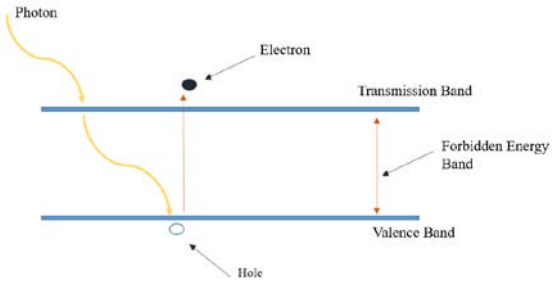


**Figure 3.7. Electron Motion and Remaining Gap Depending on Photon Energy (Istanbul Technical University, 2023).**

## 4. USE OF P-N TYPE SEMICONDUCTORS IN SOLAR CELLS

When P-type and N-type semiconductors are combined in a cell, there is an electron-dense environment in the N-type and a hole-dense environment in the P-type. Some electrons in the N-type region and some holes in the P-type region are separated from where they are in the area where the semiconductors are combined. During this separation, the electron leaves a positive charge in its place, and the hole leaves a negative charge. This process continues until the progress stops, as in Figure 4.1, and when the balance is achieved, an electric field free of carriers is formed in the intermediate area.

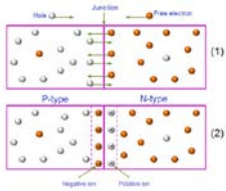


**Figure 4.1. Electric Field Created as a Result of Electron and Hole Movement (Numanoğlu, 2022).**

When sunlight hits the panel cell, electron-hole pairs are formed and the electrons that come out of these pairs to the conduction band are separated from the holes. When the two sides of the cell are connected to the load with a conductor, electricity is produced, as shown in Figure 4.2 (Numanoğlu, 2022).

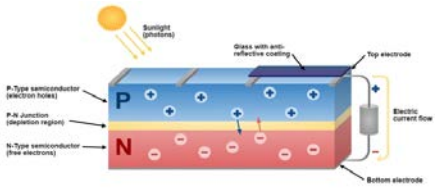


**Figure 4.2. Solar Cell Structure (Mehmet & Yetik, 2020)**

## 5. SOLAR PANELS

Panel production is carried out by combining cells (batteries) made of semiconductors in certain numbers (generally connected in series to reach the required voltage). Table 5.1 shows the percentage ratios of some semiconductor solar cells according to two environments.

**Table 5.1. Types and Efficiencies of Solar Cells (Istanbul Technical University, 2023)**

| | Percentage Efficiency | | |
|---|---|---|---|
| **Material** | **Type** | **Inside the laboratory** | **In the market** |
| **Silicon** | Monocrystalline | 24,7 | 14-18 |
| **Polysilicon** | Polycrystalline | 19,8 | 13-15 |
| **MIS Inversion Layer (Silicon)** | Monocrystalline | 17,9 | 16 |
| **Concentrator Solar Cell (Silicon)** | Monocrystalline | 26,8 | 25 |
| **Silicone on Glass Base** | Transfer Technology | 16,6 | |
| **Amorphous Silicon** | Thin Film | 13 | 8 |
| **Tandem 2 Layers, Amorphous Silicon** | Thin Film | 13 | 8,8 |
| **Tandem 3 Layers, Amorphous Silicon** | Thin Film | 14,6 | 10,4 |
| **Gallium Indium Phosphate** | Tandem Cell | 30,3 | 21 |
| **Cadmium Telluride** | Thin Film | 16,5 | 10,7 |
| **Copper Indium Di-Seleneide** | Thin Film | 18,4 | 12 |

Pure elements compatible with the sun's photon energy spectrum are silicon (1.1 eV) and germanium (0.6 eV). Other semiconductors are used as compounds. Although silicon's ability to absorb sunlight is not very good compared to others, it is widely preferred due to its greater availability on Earth and cost advantage. Panels

obtained by combining cells are examined in three or four ways (Istanbul Technical University, 2023).

### 5.1. Monocrystalline Panel

These panels are expensive due to the difficulty of production. Since their cells are made of a single, pure, and utterly crystalline silicon, electron movement is high, and therefore, they are more efficient than other panels. Although the installation cost is high, this expense is amortized over time and is a valuable option in long-term projects. As seen in the example in Figure 5.2, square types are generally preferred since round ones cause space loss in the panel (Mehmet & Yetik, 2020).

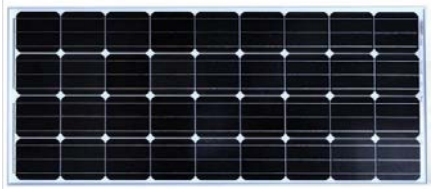

**Figure 5.1. Monocrystalline Panel Example (Mehmet & Yetik, 2020)**

### 5.2. Polycrystalline Panel

The structural difference between polycrystalline panels and monocrystalline panels is that they are formed mainly by combining melted silicon pieces. An example module is shown in Figure 5.3. The polycrystalline formation is clearly visible in bright light. Since these non-homogeneous panels are cheaper, they are produced in large quantities. There are veins between crystals in polycrystalline material. The size of these veins affects the crystal quality. Their efficiency is lower compared to monocrystalline ones (Mehmet & Yetik, 2020).

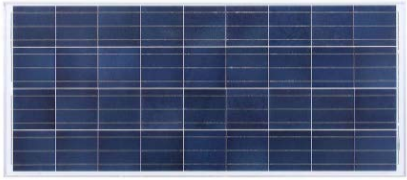

**Figure 5.2. Polycrystalline Panel Example (Mehmet & Yetik, 2020)**

### 5.3. Thin Film and Flexible Panels

These panels can absorb sunlight at a high rate. As seen in Figure 5.3, their flexible structure makes assembly easy. The efficiency rate is low in some materials. However, technological studies are aimed at increasing this rate. Especially in the space field, semiconductors such as Ga elements are used in these types of panels to create a multilayer structure.

**Figure 5.3. Thin Film Panel Example (Mehmet & Yetik, 2020)**

They perform better than other panels in places with low light, cloudy weather, and high temperatures. However, the desired level of efficiency cannot be obtained in the long term. Thin film panels (also known as thin) have varieties such as amorphous, cadmium, cadmium telluride, and copper indium di-selenide (Mehmet & Yetik, 2020).

## 6. PARAMETERS AFFECTING EFFICIENCY IN PANELS

### 6.1. Temperature - Radiation Effect and Panel Tilt Angle

With the increase in light in the panel cells, the circuit current increases, and the voltage increases very slightly. With the increase in current, the panel power also increases in the same way.

The increase in temperature reduces the open circuit voltage and increases the short circuit current by a very small amount. In other words, the high temperature reduces the total panel power and also reduces the efficiency.

As can be seen in the illustration in Figure 6.1, when the sunlight comes perpendicular to the panel, more power is produced compared to angles below this degree. Like the movement of the sunflower plant towards the sun, new technology is being developed to constantly take the light angle perpendicular (Erişgïn et al., 2022).

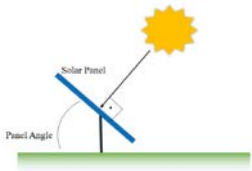


**Figure 6.1. Panel Beam Angle Display (DAL, 2021)**

When different inclination angles are taken according to the months, as in Figure 6.2, the efficiency of the panels can be kept at the highest level.

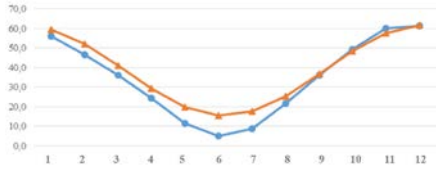


**Figure 6.2. Optimum Inclination Angles Based on Month According to Two Different Methods (DAL, 2021)**

## 6.2.Internal Resistance Loss – (Ac – Dc) Cable Losses and Cell Cleaning

The cells in the panel are usually connected in series to keep the current value constant and increase the voltage. In some productions, in order to minimize this loss, the cells are divided into two, as shown in Figure 6.3, and the current value is naturally halved. In this application, efficiency is contributed.

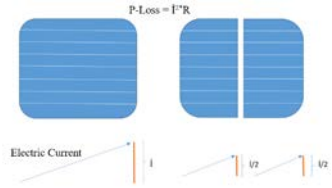


**Figure 6.3. Half Cut Cell Representation with Four-fold Decrease in Energy Loss (Duman & Alçı, 2022)**

Conductive cables are used in panel connections, and there are section resistances based on the thickness of the cables. The cables cause voltage losses depending on their length and being very thin.

Another efficiency loss that occurs in panel cells is dust and contamination due to different reasons (such as snow and falling objects). When not cleaned by blocking the rays coming from the sun, severe losses occur. Automatic cleaning robots that clean panel surfaces have

been developed with new technology. As seen in Figure 6.4, these remotely controlled robots remove even dirt that is difficult to clean with their stain detection sensors. In some studies, the loss rate due to dust can reach 15% in places where rainfall is low (Erïşgïn et al., 2022).

**Figure 6.4. Panel Cleaning Robots (Solar Clean, 2023)**

### 6.3.Shadowing, Spectrum and Mismatch Losses

Shadows falling on solar panels for specific reasons or natural cloud cover also cause a loss of efficiency. As seen in Figure 6.5, measurements made in a laboratory environment with whole light and 33% shade on a monocrystalline panel show the difference in efficiency.

**Figure 6.5. Taking Measurements While a Certain Part is Under Shadow (Mehmet & Yetik, 2020)**

While the output voltage is measured as 18.88 V when the panel is fully exposed to light, a voltage value of 7.53 V is observed under shade.

Photovoltaic cells can show different sensitivity to the spectral band range of light. Cells using CIS (copper indium selenide) and C-Si (crystalline silicon) materials

have a much broader range in spectral response than other materials.

If the modules within the array of panels have different aging factors, operate at different temperature values, have different light-receiving data and angles, and have different cables with different lengths and cross-sections, all these cause losses due to incompatibility (Eşref, 2023).

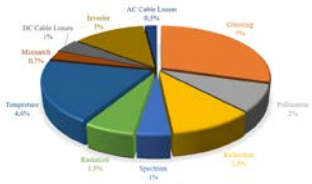

**Figure 6.6. Ratios of Losses in Solar Panels According to Total DC Production (Erişgïn et al., 2022)**

## 7. RESULTS

In this study, various structural and performance features of the cells currently used frequently in solar panels, which are gaining momentum in the production of electricity from the sun, a renewable energy source, have been examined. In the current period, the advantages and disadvantages of these cells over each other have been analyzed as a result of R&D activities carried out in the developing technology.

The place of semiconductors in the solar energy system, the purposes for which they are used, and the essential features that distinguish them from other materials are emphasized, and their relationship with photon energy is explained in detail.

Although the energy obtained from the sun has advantages such as zero-emission, silent operation, direct energy production, and devices that use other renewable energy sources that do not require significant maintenance, some aspects pose a threat to the environment and health if the materials used are not recycled when their lifespan ends. For this reason, companies continue to operate by evaluating panel scraps and converting them back into various materials. Aluminum, glass, and the materials contained therein are separated to a certain extent, and their transformation is ensured.

Other semiconductors used together with the Ga element in solar cells can be formed in a multi-junction structure, and their performance values can be maximized by increasing the number of these junctions. If the costs of these materials and the cells they are used in decrease over time with developing technology, they can be used outside of defense and space technologies.

**REFERENCES**

Ankara University. (2023). Solid State Physics. Retrieved 10 December 2023 from https://acikders.ankara.edu.tr/pluginfile.php/136634/mod_resource/content/0/03-yar%C4%B1iletken1.pdf

Ashraf, D. (n.d.). *Losses in Solar Power Plants*. Retrieved 18 December 2023 from https://www.emo.org.tr/ekler/38f0038bf09a40b_ek.pdf

Dal, A. R. (2021). Investigation of the Effect of Optimum Tilt Angle on Efficiency in Solar Energy Panels. *Bilecik Şeyh Edebali University Journal of Science*, 8(1), 241–250. Retrieved 17 December 2023 from https://doi.org/10.35193/bseufbd.878795

Duman, S., & Gypsum, M. (2022). Investigation of the parameters affecting the total efficiency of solar panels designed with half and full photovoltaic cells. *Science. Derg. / NOHU J. Eng. Sci*, 11(3), 592–600. Retrieved from https://doi.org/10.28948/ngmuh.1073976

Electronic Properties of Semiconductors. (2023). *Semiconductor materials*. Retrieved 9 December 2023 from https://acikders.tuba.gov.tr/pluginfile.php/1073/mod_resource/content/1/Bolum-12.pdf.

Erişgin, D., Kara, G., Özcan, H., Mayıs University Faculty of Engineering, O., Department of Engineering, M., Mayıs University, O., ... See Gürkan KARA, A.

(2022). Investigation of the Effects of the Use of Surface Acoustic Waves on Photovoltaic Panel Performance in Photovaltaic Panel Cleaning. Retrieved 3 December 2023 from https://ojs.omu.edu.tr/jest/article/view/60/13

Istanbul Technical University. (n.d.). History of Solar Cells. Retrieved 9 December 2023 from https://web.itu.edu.tr/~kaymak/PV.html

Mehmet, Ö. U., & Yetik, K. (2020). Effects and Analysis of The *Ratios Between Sun And Shade On Efficiency in Solar Panels*. Retrieved 3 December 2023 from http://acikerisim.karabuk.edu.tr:8080/xmlui/bitstream/handle/123456789/999/10369736.pdf?sequence=1&isAllowed=y

Numanoğlu, M. (n.d.). *Conductive, Insulating And Semiconductor Materials*. Retrieved 15 December 2023 from https://acikders.ankara.edu.tr/pluginfile.php/154970/mod_resource/content/0/5.%20%C4%B0letken%2C%20Yal%C4%B1tkan%20ve%20Yar%C4%B1%20%C4%B0letken%20Maddeler.pdf#:~:text=P%2DN%20yar%C4%B1%20iletkenleri%20birle%C5%9Fince%20birle%C5%9Fim,pozitif%20iyon%20(%2B)%20durumna%20ge%C3%A7erler.

Solar Cell - What is a Solar Battery? (2023). *Https://Www.Antalyaenerji.Com/Gunes-Fotovoltaik-Pili-Nedir-ve-Nasil-Calisir/*.

Solar Clean. (n.d.). Solar Clean. Retrieved 18 December 2023 from https://solarcleano.com/tr/gallery

Tunçkaşik, İ., & Köse, E. (2022). Evaluation of the Effect of Different Designs on Efficiency in Photovoltaic Panels. *European Journal of Science and Technology*. Retrieved 3 December 2023 from https://doi.org/10.31590/ejosat.1165188.

# STUDY OF STRUCTURAL AND ELECTRONIC PROPERTIES OF *h*-BN USING AB-*INITIO* METHODS

**Cengiz SOYKAN**[1]

## 1. INTRODUCTION

Boron nitride (BN) is a semiconductor material that stands out with its various polymorphic structures and diverse potential applications. Among these, cubic boron nitride (c-BN) has been extensively studied due to its remarkable thermodynamic properties, such as extreme hardness, chemical inertness, high melting point (under high pressure), excellent thermal conductivity, and wide band gap. These properties make c-BN an ideal material for numerous industrial applications, including abrasives, protective coatings, and microelectronic devices. Recently, another polymorph, hexagonal boron nitride (*h*-BN), has been successfully synthesized as a single crystal with a direct band gap of 5.97 eV (Watanabe et al., 2004; Evans et al., 2008; Zupan et al., 1972; Zunger et al., 1976; Hoffman et al., 1984). This characteristic enables ultraviolet laser emission at 215 nm, paving the way for innovative technologies such as compact ultraviolet lasers, optical data

[1] Assoc. Prof. Dr., Kırşehir Ahi Evran University, Health Services Vocational School, Department of Medical Services and Techniques, cengiz.soykan@ahievran.edu.tr, ORCID: 0000-0003-0897-2384.

storage, photocatalysis, and medical devices (Hamdi et al., 2010; Gao et al., 2012; Watanabe et al., 2004).

The properties of *h*-BN are of great significance not only due to its graphite-like structure and structural stability but also because of its electronic characteristics. This material has become an important subject of research in both fundamental science and applied fields. Understanding the structural and electronic properties of *h*-BN can contribute to the design of next-generation electronic and optoelectronic devices. In particular, its wide band gap and high thermal stability make *h*-BN an ideal candidate for high-performance optoelectronic devices (Gao et al., 2012; Xu et al., 1991; Furthmüller et al., 1994; Liu et al., 2003; Cappellini et al., 2000; Blase et al., 1995).

The crystal structure of *h*-BN consists of boron and nitrogen atoms arranged in AB-stacked planes. These layers are held together by weak Van der Waals forces, making *h*-BN mechanically flexible and resistant to high temperatures. Electrically, *h*-BN is an insulating material due to its wide band gap; however, this property also makes it suitable for high-performance optical applications. In recent years, studies on the band structure of *h*-BN have further expanded its potential applications (Zupan et al., 1972; Zunger et al., 1976; Hoffman et al., 1984).

This book chapter aims to provide an in-depth analysis of the structural and electronic properties of *h*-BN. First, the crystal structure of *h*-BN will be simulated based on the computational criteria outlined in the Methods section. Structural properties such as the lattice constants, volume, and bulk modulus of the optimized crystal

structure will be reported. Subsequently, based on the optimized crystal structure, the phase's total and partial density of states (DOS and pDOS) will be investigated. In light of the obtained data, the electronic properties of the structure, particularly electronic parameters such as the band gap and conductivity, will be discussed. The findings will be compared with both theoretical calculations and experimental results, and the conclusions will be reported accordingly.

## 2. METHOD

In this study, ab-*initio* (first-principles) calculations were performed to determine the structural and electronic properties of *h*-BN. The calculations were based on Density Functional Theory (DFT) and carried out using the CASTEP software package (Clark et al., 2005; Kresse et al., 1996; Kresse et al., 1996; Kresse et al., 1994). The exchange-correlation function was considered using the Generalized Gradient Approximation (GGA) with the Perdew-Burke-Ernzerhof (PBE) functional approach (Perdew et al., 1996). This approach is widely used for accurately modeling the electronic structures of two- and three-dimensional materials and is particularly suitable for wide band gap materials such as *h*-BN.

The structural properties of *h*-BN were optimized according to criteria set as follows: energy tolerance of $10^{-5}$ eV/atom, maximum force of 0.03 eV/Å, maximum stress of 0.05 GPa, and maximum displacement of 0.001 Å (Fischer et al., 1992). To ensure the accuracy of the calculations, an energy cutoff value of 500 eV was selected.

This energy value enhances the precision of the crystal structure parameters, ensuring the reliability of the computations.

The k-point distribution in the Brillouin zone was set to 12x12x10 (Monkhorst et al., 1976). This k-point density balances the speed and accuracy of the calculations, ensuring the precise determination of *h*-BN's structural parameters. As a result of the structural optimizations, the lattice constants (a, b, c, Å) and volume (V, Å$^3$) of *h*-BN were obtained. Additionally, the optimizations enabled the energy minimization of *h*-BN, identifying the configuration with the lowest energy.

For the calculations of the electronic band structure and density of states (DOS), the k-point density was increased to 36x36x12. This higher k-point density allows for more precise and accurate determination of the band structure and DOS (Hohenberg et al., 1964; Kohn et al., 1965).

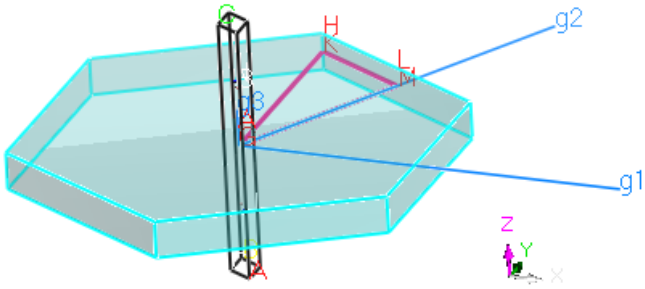


**Figure 1. First Brillouin zone of P6$_3$/mmc lattice, showing symmetry labels for high symmetry lines and points of hexagonal *h*-BN.**

As shown in Figure 1, the electronic band structure calculations were performed along a path starting from the

gamma point ($\Gamma$), proceeding to the $K$ point, then to the $M$ point, and returning to $\Gamma$ ($\Gamma \rightarrow K \rightarrow M \rightarrow \Gamma$). These calculations at specific k-points enabled a detailed analysis of the electronic structure of *h*-BN. This approach allows for a more precise examination of *h*-BN's band structure and facilitates the comparison of different crystal structures (Hohenberg et al., 1964; Kohn et al., 1965; Payne et al., 1992).

When examining the structural and electronic properties of *h*-BN, the electronic configurations of the B and N atoms were also considered. The electronic configuration of the B atom is [He] $2s^2$ $2p^1$, while that of the N atom is [He] $2s^2$ $2p^3$. These configurations are fundamental determinants of the electronic structure of h-BN and play a critical role in understanding the semiconductor properties of the material. To ensure the accuracy of the calculations, the structural parameters of *h*-BN were compared with experimental data from the literature, and the obtained results were found to be in good agreement with the experimental values (Watanabe et al., 2004; Evans et al., 2008). Additionally, the calculated electronic parameters were compared with previous theoretical studies in the literature, and similar results were obtained (Blase et al., 2004; Gao et al., 2012). These results confirm the reliability and accuracy of the computational method.

## 3. RESULTS AND DISCUSSION

The crystal structure of *h*-BN is a hexagonal arrangement defined by the $P6_3/mmc$ space group. The shape of the crystal structure is shown in Figure 2 below.

This structure is characterized by the equicoordinated arrangement of boron (B) and nitrogen (N) atoms, which form covalent bonds, with boron atoms bonding to each nitrogen atom. The van der Waals interactions between the layers give rise to weak interlayer forces in the structure. As a result, *h*-BN exhibits mechanical stability and, due to its layered structure, can be easily exfoliated. While this provides properties similar to graphene, it leads to distinct differences in its electronic characteristics.

The lattice parameters of the hexagonal crystal structure have been calculated as a = b = 2.548 Å and c = 7.597 Å. These calculated structural properties are presented in Table 1 below for comparison with theoretical and experimental studies. The obtained values are in good agreement with other theoretical and experimental works in the literature. When compared to the experimentally reported values by Solozhenko and Bosak, which are a = b = 2.504 Å and c = 6.660 Å, it is observed that the calculated c-axis is slightly longer in this study (Solozhenko et al., 1995; Bosak et al., 2006). This difference is thought to arise from the computational methodology and energy cutoff values used.

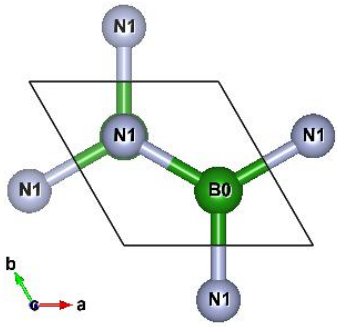


**Figure 2. The crystal structure of hexagonal *h*-BN.**

Similarly, when compared to theoretical results, the values in this study are close to the results reported by Janotti, which are a = b = 2.517 Å and c = 8.397 Å (Janotti et al., 2001).

**Table 1. The lattice parameters of h-BN.**

| Cry. | | Lattice Constans ($A^0$), a, b, c | | | Volume ($A^3$) | Ref. |
|---|---|---|---|---|---|---|
| | Teo. | 2.548 | 2.548 | 7.597 | 24.66 | This work |
| | Teo. | 2.494 | 2.494 | 6.660 | | Xu |
| | Teo. | 2.502 | 2.502 | 6.902 | | Gao |
| | Teo. | 2.517 | 2.517 | 8.397 | | Janotti |
| | Exp. | 2.504 | 2.504 | 6.660 | | Solozhenko |
| *h*-BN | Exp. | 2.506 | 2.506 | 6.657 | | Bosak |
| | Exp. | 2.500 | 2.500 | 6.660 | | Fuchizaki |

One of the characteristic features of the layered structure, the low interlayer forces, significantly affects the physical properties of this material. Specifically, the c/a ratio is an indicator of the anisotropic properties of the material, and the calculated c/a = 2.98 in this study is very close to the values reported in the literature. This ratio confirms that *h*-BN exhibits non-isotropic electronic and mechanical properties, similar to graphene.

Another notable feature of the structure is the longer interlayer distance (approximately 3.3 Å) compared to graphene. This characteristic reduces the interlayer electron interactions and contributes to the wide bandgap of *h*-BN. Additionally, the high electronegativity of nitrogen atoms increases the bond polarity in the formation of bonds with boron atoms, which stands out as one of the main reasons for the differences in the electronic properties.

In this study, the accuracy of the calculated lattice parameters and unit cell volume is largely consistent with the literature, demonstrating the reliability of first-principles methods. Additionally, the structural stability of *h*-BN, along with its ability to maintain stability even at high temperatures, makes it an ideal material for high-performance electronic and optoelectronic devices.

**Table 2. The calculated band gaps of *h*-BN crystal structures and the other theoretical and experimental data.**

| Cry. | | Band gap (*eV*) | Transition types | Ref. |
|---|---|---|---|---|
| *h*-BN | Teo. | 4.434 | Direct | This work |
| | Teo. | 5.002 | Indirect | Gao |
| | Teo. | 4.676 | Indirect | We |
| | Exp. | 5.971 | Direct | Watanabe |
| | Exp. | 5.960 | Direct | Evans |

In this study, the calculated band gap and other theoretical and experimental studies are compared and presented in Table 2 above. As shown in Figure 3 below, the band gap of *h*-BN is found through the K symmetry point. This indicates that the *h*-BN crystal has a direct band gap. The direct band gap is calculated to be 4.434 eV. Since the band structure shows a direct band gap transition from the K point to the K point ($K \rightarrow K$), this value is particularly important for optoelectronic applications. This is because the structure can be excited electronically by a photon alone, without the need for phonon excitation. This finding confirms that *h*-BN is an ideal material for applications such as light emission due to its wide band gap.

The band gap calculated in this study shows both similarities and differences when compared to theoretical

and experimental studies in the literature. Theoretical calculations by Gao and We report band gaps of 5.002 eV (indirect) and 4.676 eV (indirect), respectively (Gao et al., 2012; We et al., 2011). When compared with experimental data, Watanabe and Evans measured direct band gaps of approximately 5.971 eV and 5.960 eV, respectively, in their studies. These values are higher than our results. The variability in band gap values is due to differences in the calculation methods used. For instance, DFT-GGA-based methods tend to slightly underestimate the band gap, while more complex methods (such as GW and Bethe-Salpeter) may provide more accurate predictions of the band gap. However, it is well known that DFT methods generally predict band gaps smaller by about 1 eV compared to experimental values. This behavior, however, can vary depending on the space symmetry of the calculated crystal structure and the accuracy of the computation (Sholl et al., 2009).

As shown in Figure 4 below, the contributions of Boron (B) atoms' s and p orbitals play a significant role in the formation of the electronic structure of *h*-BN. The contribution of Boron atoms' s orbitals primarily affects the valence band at lower energy levels, while the p orbitals contribute to both the low-energy valence band and the high-energy conduction band. This feature has a decisive impact on the symmetry and character of *h*-BN's band structure.

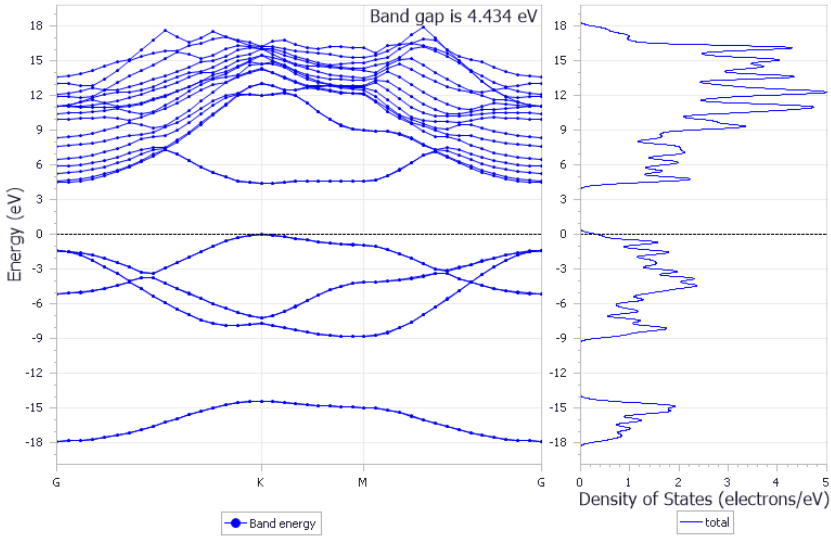


**Figure 3. Calculated electronic band structures and density of states (electrons/eV) for *h*-BN at 0 GPa.**

Specifically, the contributions of the p orbitals of B atoms direct the orbital interactions that form π bonds, situated between the valence band and the conduction band. These interactions are a key factor in shaping sharp transitions in the band structure, particularly the energy gaps. The p orbitals of B atoms interact with the p orbitals of N atoms, determining the energy levels of the π and π* orbitals formed due to $sp^2$ hybridization. This interaction plays a crucial role in defining the semiconducting properties and the wide band gap of *h*-BN (Gao et al., 2016; Watanabe et al., 2004).

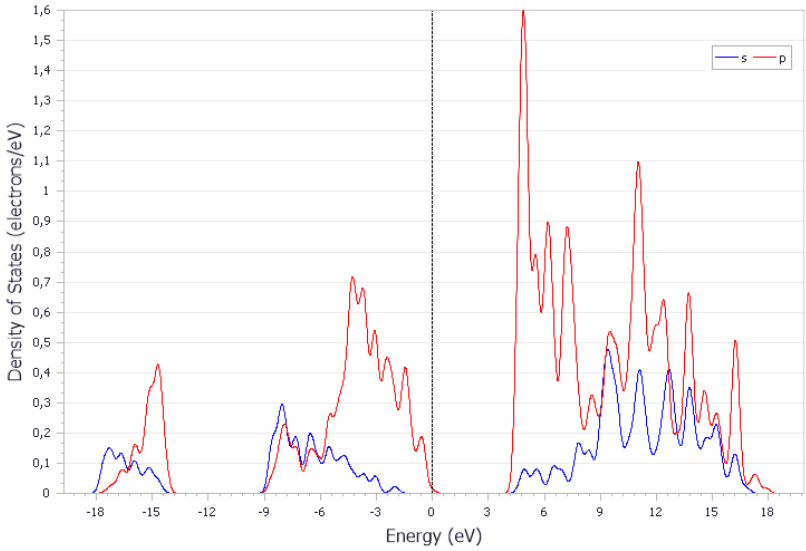


**Figure 4. Calculated partial density of states (electrons/eV) for *h*-BN at zero pressure. The vertical dot line represents the Fermi level shifted to 0 eV. The main bonding peaks of *h*-BN are originated from the contribution of valence electron numbers of B (2s2p) orbits.**

The contributions of the s orbitals of B atoms, on the other hand, are primarily used to form σ bonds that stabilize the crystal structure. These bonds help stabilize the $sp^2$ hybridized bonds between boron and nitrogen atoms and ensure the formation of strong covalent bonds between the layers. While these σ bonds are crucial for the mechanical strength of *h*-BN, they do not significantly alter the band structure (We et al., 2011; Blase et al., 2004). The formation of the band structure can be better understood through calculations that account for the contributions of the B atom's orbitals. The π* orbitals determine the mobility of charge carriers in the conduction band, which is crucial for the high optical properties and high conductivity of h-BN. These contributions make h-BN particularly attractive

for applications such as optoelectronic devices and laser technologies.

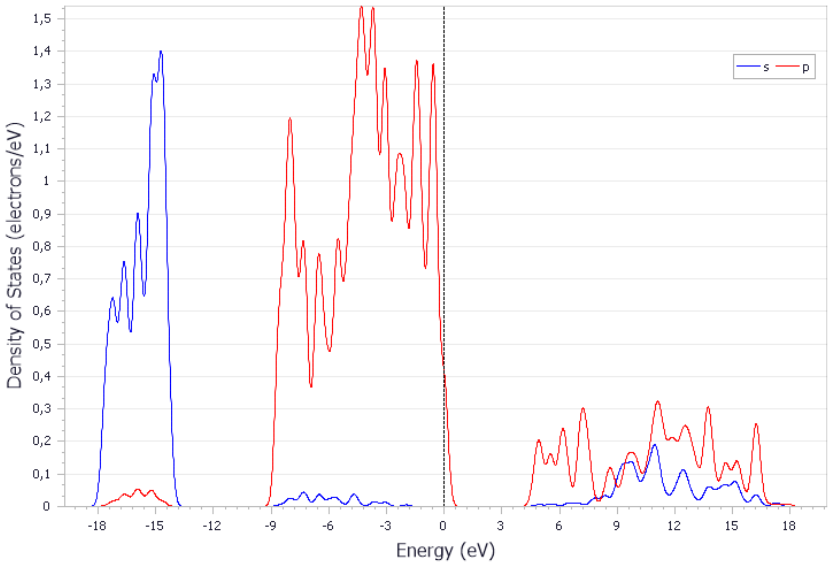


**Figure 5. Calculated partial density of states (electrons/eV) for *h*-BN at zero pressure. The vertical dot line represents the Fermi level shifted to 0 eV. The main bonding peaks of *h*-BN are originated from the contribution of valence electron numbers of N (2s2p) orbits.**

As shown in Figure 5, the contributions of nitrogen (N) atoms to the electronic structure of *h*-BN are particularly noticeable through interactions with p orbitals, and these contributions play a critical role in shaping the electronic properties of *h*-BN. Due to $sp^2$ hybridization, nitrogen atoms use their p orbitals for the π bonds in the valence band, which is an important characteristic of the band structure (Gao et al., 2016; Watanabe et al., 2004). These nitrogen orbitals affect both the valence band and the conduction band. The contributions of N atoms interact with the s and p orbitals of the B atoms, determining the π

and π* energy levels. These bonds enable the semiconductor properties of *h*-BN and enhance the conductivity of charge carriers (Gao et al., 2016; Watanabe et al., 2004). The p orbitals of nitrogen atoms influence the transitions between the valence band maximum (VBM) and conduction band minimum (CBM), shaping the characteristic band structure of *h*-BN. Through the contributions of π bonds and π*, nitrogen atoms play a crucial role in creating significant charge carriers in the conduction band. This property is directly linked to the wide band gap and optical characteristics of *h*-BN (Gao et al., 2016; Watanabe et al., 2004). In conclusion, the contribution of nitrogen atoms to the electronic structure plays a central role in shaping the electronic properties of *h*-BN, providing a strong foundation for optical and electronic applications.

**REFERENCES**

Blase, X., Rubio, A., Louie, S. G., & Cohen, M. L. (1995). Phys. Rev. B, 51(12), 6868. https://doi.org/10.1103/PhysRevB.51.6868

Bosak, A., Serrano, J., Krisch, M., Watanabe, K., Taniguchi, T., & Kanda, H. (2006). Phys. Rev. B, 73(4), 041402(R). https://doi.org/10.1103/PhysRevB.73.041402

Cappellini, G., Satta, G., Tenelsen, K., & Bechstedt, F. (2000). Phys. Status Solidi B, 217(4), 861.

Clark, S. J., et al. (2005). First principles methods using CASTEP. Zeitschrift für Kristallographie-Crystalline Materials, 220(5-6), 567-570. https://doi.org/10.1524/zkri.220.5.567.65075

Evans, D. A., McGlyn, A. G., Towlson, B. M., Gunn, M., Jones, D., Jenkins, T. E., Winter, R., & Poolton, N. R. J. (2008). J. Phys: Condens. Matter, 20(7), 075233. https://doi.org/10.1088/0953-8984/20/7/075233

Fischer, T. H., & Almlof, J. (1992). General methods for geometry and wave function optimization. The Journal of Physical Chemistry, 96(24), 9768-9774. https://doi.org/10.1021/j100202a074

Furthmüller, J., Hafner, J., & Kresse, G. (1994). Phys. Rev. B, 50(15), 15606. https://doi.org/10.1103/PhysRevB.50.15606

Gao, S.-P. (2012). Crystal structures and band gap characters of h-BN polytypes predicted by the dispersion-corrected DFT and GW method. Solid

State Communications, 152(16), 1817–1820. https://doi.org/10.1016/j.ssc.2012.07.022

Hohenberg, P., & Kohn, W. (1964). Inhomogeneous electron gas. Physical Review, 136(B864-B871). https://doi.org/10.1103/PhysRev.136.B864

Hoffman, D. M., Doll, G. L., & Eklund, P. C. (1984). Phys. Rev. B, 30(10), 6051. https://doi.org/10.1103/PhysRevB.30.6051

Janotti, A., Wei, S.-H., & Singh, D. J. (2001). Phys. Rev. B, 64(17), 174107. https://doi.org/10.1103/PhysRevB.64.174107

Kresse, G., & Furthmüller, J. (1996). Efficiency of ab-*initio* total energy calculations for metals and semiconductors using a plane-wave basis set. Computational Materials Science, 6(1), 15-50. https://doi.org/10.1016/0927-0256(96)00008-0

Kresse, G., & Furthmüller, J. (1996). Efficient iterative schemes for ab-*initio* total-energy calculations using a plane-wave basis set. Physical Review B, 54(16), 11169. https://doi.org/10.1103/PhysRevB.54.11169

Kresse, G., & Hafner, J. (1994). Norm-conserving and ultrasoft pseudopotentials for first-row and transition elements. Journal of Physics: Condensed Matter, 6(40), 8245. https://doi.org/10.1088/0953-8984/6/40/010

Kohn, W., & Sham, L. J. (1965). Self-consistent equations including exchange and correlation effects. Physical Review, 140(A1133-A1138). https://doi.org/10.1103/PhysRev.140.A1133

Liu, L., Feng, Y. P., & Shen, Z. X. (2003). Phys. Rev. B, 68(10), 104102. https://doi.org/10.1103/PhysRevB.68.104102

Monkhorst, H. J., & Pack, J. D. (1976). Special points for Brillouin-zone integrations. Physical Review B, 13(12), 5188. https://doi.org/10.1103/PhysRevB.13.5188

Payne, M. C., Teter, M. P., Allan, D. C., Arias, T. A., & Joannopoulos, J. D. (1992). Iterative minimization techniques for ab initio total-energy calculations - molecular dynamics and conjugate gradients. Reviews of Modern Physics, 64(4), 1045–1097. https://doi.org/10.1103/RevModPhys.64.1045

Perdew, J. P., Burke, K., & Ernzerhof, M. (1996). Generalized gradient approximation made simple. Physical Review Letters, 77(18), 3865. https://doi.org/10.1103/PhysRevLett.77.3865

Sholl, D. S., & Steckel, J. A. (2009). Density functional theory: A practical introduction (p. 28). Wiley.

Solozhenko, V. L., Will, G., & Elf, F. (1995). Solid State Commun., 96(1), 5-9.

Watanabe, K., Taniguchi, T., & Kanda, H. (2004). Nat. Mater., 3(6), 404.

We, Y., Zhang, L., & Li, X. (2011). Theoretical studies of the structural, electronic, and thermodynamic properties of boron nitride polymorphs. Physical Chemistry Chemical Physics, 13(32), 14565–14570. https://doi.org/10.1039/C1CP20435A

Xu, Y.-N., & Ching, W. Y. (1991). Phys. Rev. B: Condens. Matter, 44(15), 7787. https://doi.org/10.1103/PhysRevB.44.7787

Zunger, A., Katzir, A., & Halperin, A. (1976). Phys. Rev. B, 13(10), 5560. https://doi.org/10.1103/PhysRevB.13.5560

Zupan, J., & Kolar, D. (1972). J. Phys. C, 5(14), 3097.

# EVALUATION OF INTRINSIC HARDNESS PARAMETERS OF ZNO SEMICONDUCTOR ADDED BI-2223 CERAMIC STRUCTURES BY MECHANICAL METHODS[1]

**Tahsin TURGAY** [1]

**Ümit ERDEM** [2]

**Mustafa Burak TÜRKÖZ**[3]

## 1. INTRODUCTION

It is well known that the Bi-2223 ceramic prepared within the stoichiometry of $Bi_2Sr_2Ca_2Cu_3O_{10+\delta}$ exhibits a number of advantages over other superconducting phases that make the type-II superconductor particularly valuable for a number of high-performance applications. The Bi-2223 phase has a higher critical temperature, typically around 110 K (Hilgenkamp & Mannhart, 2002; Erden, Tasliyan, & Akgul, 2021; Pul, 2018). Thus, the suitable practical and engineering applications of the material are relatively lower cost due to the cooling costs and operational temperatures, as compared to the other

[1] Prof. Dr. Sakarya University, Departments of Architecture, tahsinturgay@gmail.com, ORCID: 0000-0003-0304-1097.

[2] Assoc. Prof. Dr. Kırıkkale University, Kırıkkale Vocational School, Department of Electronıcs and Automation, erdem.umit@gmail.com, ORCID: 0000-0002-0480-8176.

[3] Assoc. Prof. Dr. Karabuk University, Faculty of Engineering, Electric-Electronics Engineering, mbturkoz@karabuk.edu.tr, ORCID: 0000-0002-4127-7650.

superconductors. Besides, since the Bi-2223 phase can carry greater critical current density (Jc) than $10^5$ A/cm², the compounds seem to be ideal for applications requiring the transmission of large electrical currents, such as power cables, fault current limiters, and superconducting magnets. The Bi-2223 phase has enhanced flux pinning/stabilization capabilities that help the material maintain its superconducting properties in the presence of high applied magnetic field strengths, making the material particularly useful in applications such as magnetic levitation, advanced magnet technologies, and other areas involving strong magnetic fields. Bi-2223 also exhibits better high mechanical strength and flexibility properties compared to other participants in its family. Due to the mentioned attractive properties, the ceramic compound can be used in applications requiring long lengths of superconducting tapes and wires that can withstand mechanical stress, such as superconducting cables for electrical networks (Ateş, 2016). Further, Bi-2223 is more amenable to tape processing techniques such as rolling and coating processes used to produce long-length superconducting tapes. This is why the material is widely preferred in industrial applications where large amounts of superconducting material are required. At the same time, the Bi-2223 presents lower alternating current (AC) losses compared to other superconductors; accordingly, the usage of material in applications such as transformers and AC power transmission increases seriously system efficiency. Moreover, the Bi-2223 phase remains stable under various operating conditions, such as different environmental temperatures and applied magnetic field strengths ranges.

The serious stability at relatively higher temperatures improves the performance in practical environments and reduces the complexity of cooling requirements. In this context, the Bi-2223 superconductive phase with higher critical temperature, current, and external magnetic field carrying capabilities is used in HTS devices such as motors, generators, and magnetic resonance imaging (MRI) systems where high performance at high temperatures is desired.

Further, the Bi-2223 superconducting phase with layered anisotropic micaceous, granular structure, inter-granular boundaries, and randomly oriented microcrystals has serious brittleness feature and thus exhibits relatively lower mechanical stabilization (Plakida, 2010; Ateş, 2016; Altunpak, Aslan, Guler, & Akbulut, 2016; Altunpak, & Ülgen, 2023). Correspondingly, it is essential to comprehend how the mechanical assets vary when ZnO semiconductor impurity ions are added to Bi-2223 ceramics and inspect the practical uses of the materials in various industries (Ateş, 2013). This work aims to improve the economic life of Bi-2212 ceramic compound by addition of ZnO particles in the lattice, thereby expanding potential application fields of the Bi-2223 ceramics (Ozkurt, 2014).

The crystal structure, characterized by van der Waals bonds in the BiO planes, allows for easy deformation, making them suitable for long cable constructions and tape casting (Michels, & Frischat, 1982; Li, & Bradt, 1993). The material is stable against compositional changes, resistant to water and humidity, and compatible with cooling systems. Besides, the high

sintering temperatures of around 840-860 °C further augment its suitability for harsh conditions (Hays, & Kendall, 1973; Tarkanian, Neumann, & Raymond, 1973; Michels, & Frischat, 1982). Additionally, the Bi-2223 superconducting phase is mechanically robust, with flexibility and strain resilience that distinguish this phase from other superconductors, making the compound promising for technological and industrial applications. Addressing intrinsic structural problems by adding different ions can improve the resistance to high current, magnetic fields, and mechanical stress, expanding the application potential of superconducting ceramics (Li, & Bradt, 1996; Sangwal, 2000; Altunpak, & Akbulut, 2009; Akkurt, & Yildirim, 2016; Altunpak, & Akbulut, 2017). Similarly, one can see detailed examinations on the semiconductor materials (Haskul, Ülgen, & Döner, 2020; Haskul, 2020).

The Vickers microhardness ($H_v$) test is widely used to evaluate basic mechanical properties; namely, hardness, yield strength, fracture toughness, ductility, and brittleness. The $H_v$ measurement testing is particularly valuable for delicate components since the experiments provide precise measurements at the micro level, detects fine defects and leaves minimal indentation. It is suitable for a variety of materials, including metals, ceramics, polymers, and composites, and is effective in analyzing individual phases or surface layers in heterogeneous materials. The adaptability of the $H_v$ method makes the material indispensable for advanced superconducting ceramic materials.

Additionally, experimental modeling helps predict the performance of any material by combining theory and experimental data accurately and effectively using semi-empirical models. These models reduce the need for costly real-world testing by identifying trends and are used to evaluate corrosive environments, service conditions, and mechanical stresses. Although similar studies exist, the use of semi-empirical mechanical modeling has not yet been sufficiently explored and requires further investigation (Sheahen, 2002; Oh, Kim, Jeong, Hyun, & Kim, 2007; Yaşar & Altunpak, 2009). This study investigates how the ZnO semiconductor impurity ions affect the mechanical properties of Bi-2223 superconducting ceramics under loads ranging from 0.245 N to 2.940 N. The research focuses on changes in stress, elastic recovery and mechanical properties such as ISE and reverse RISE features under fatigue, fracture and failure. Additionally, we study the effect of ZnO ions on granularity, crystallinity and stress distribution in the Bi-2223 advanced material. The best mechanical performance is detected for the pure sample.

This book chapter, for the first time, conducts a detailed analysis of real $H_v$ coefficients in PL (plateau limit) areas for ZnO-added Bi-2223 ceramic structures using various methods including indentation-induced cracking (IIC), Hays-Kendall (HK), Meyer law (ML), elastic/plastic deformation (EPD), proportional specimen resistance (PSR) and modified PSR (MPSR). The findings show that the IIC method is the most effective approach to evaluate Hv parameters in PL regions.

## 2. EXPERIMENTAL PROCEDURES AND COMPUTATIONS

ZnO semiconductor added Bi-2223 materials are produced using the ceramic manufacturing route. Ultra-high purity chemical powders (99.99% or higher) including $Bi_2O_3$, CuO, $SrCO_3$, $CaCO_3$, and ZnO are used throughout the production. The powders are carefully weighed according to the stoichiometric formulation ($Bi_{2.1}Sr_{2.0}Ca_{2.1}Cu_{3.0}O_y$+$ZnO_x$) and ground for 9 hours to ensure homogeneity and after then re-ground in an agate for 30 minutes to increase surface contact and promote bond formation within the ZnO doped Bi-2223 matrices.

The obtained homogeneous powder mixture is calcined at 800 °C for 36 h to optimize the formation of Bi-2223 phase, and the heating and cooling rates are maintained at 5 °C per minute. The preheated powders are then pressed into rectangular rods (1.5 × 0.5 × 0.2 $cm^3$) under 300 MPa pressure for 5 min and sintered at 850 °C for 36 h to facilitate the complete development of the Bi-2223 ceramic structure. The samples differentiated with respect to the varying ZnO additions are named as ZnBi0, ZnBi1, ZnBi2, ZnBi3, ZnBi4, and ZnBi5, corresponding to x = 0, 0.01, 0.02, 0.04, 0.08, and 0.12, respectively.

The basic mechanical performances belonging to $Bi_{2.1}Sr_{2.0}Ca_{2.1}Cu_{3.0}O_y$+$ZnO_x$ samples is evaluated under various loads ranging from 0.245 N to 2.940 N via $H_v$ testing. A pyramidal indenter is used to form impressions on the sample surfaces and data are collected for five measurements of 10 s each to ensure accuracy. The correlation between the applied loads and the resulting

indentation dimensions is analyzed to determine the Vickers hardness parameters.

In addition, the study investigates the mechanical characteristic properties (ISE or RISE) based on elastic and plastic deformation behaviors under different stress conditions using experimental hardness curves and semi-empirical mechanical models including HK, IIC, ML, PSR, EPD and MPSR methodologies. The load-independent Vickers $H_v$ values in the PL regions are theoretically investigated by the standard mechanical approaches and the effectiveness of modeling techniques in investigating the mechanical properties of ZnO added Bi-2223 ceramics is demonstrated.

## 3. RESULTS AND DISCUSSION

This study summarizes how varying levels of ZnO impurity ions and external forces (0.245 N to 2.940 N) impact the mechanical properties of Bi-2223 cuprates. Experimental results indicate that increasing ZnO content and higher loads reduce considerably general mechanical performances due to increased new crystal structure faults including impurity residues, grain misalignment, layer connection problems, stress raisers for cracks, and microvoids (Yamauchi & Karppinen, 2000). The pure Bi-2223 ceramic demonstrates better mechanical stability, strength, crystallinity, and resistance to external loads compared to other ZnO-added ceramics prepared. We also discuss shortly how substitution affects elastic recovery, phase transformations, and the degree of granularity. The focus is on load-independent hardness results in the PL

regions, using theoretical mechanical examinations (HK, IIC, ML, PSR, EPD, MPSR) to analyze deformation mechanisms. The findings provide insight into mechanical responses and changes induced by ZnO semiconductor impurity ions in the Bi-2223 ceramic system.

### 3.1. Determination of $H_v$ values for ZnO-added Bi-2223 compounds

$H_v$ measurements in this work is used to analyze the correlation between the formation of stress raisers, intergranular interactions, artificial force barriers, and shear systems. The aim is to understand how the semiconductor addition affects the mechanical strength and performance in ceramic structures. The conversion of test loads (F) and diagonal depths (d) to $H_v$ values is shown by a specific equation given below:

$$H_V = \frac{2F\sin(\alpha/2)}{d^2} = 1.8544(\frac{F}{d^2}) \quad (1)$$

In this study, d represents average diagonal depths, F denotes applied loads (N), *a* is 136°, and so 2Sin(α/2) is equal to 1.8544. Figure 1 shows that ZnO addition levels significantly affect the durability and mechanical strength of the Bi-2223 crystal system by enhancing factors such as the variation of the artificial force barriers, impurity residues, chemical bonding, grain mis/alignment, stress raisers for cracks, crystal quality, microvoids, intergranular interactions, layer interaction problems, and active slip systems. A similar situation is observed in composite materials based on the vibrational experiments (Haskul, & Kisa, 2021).

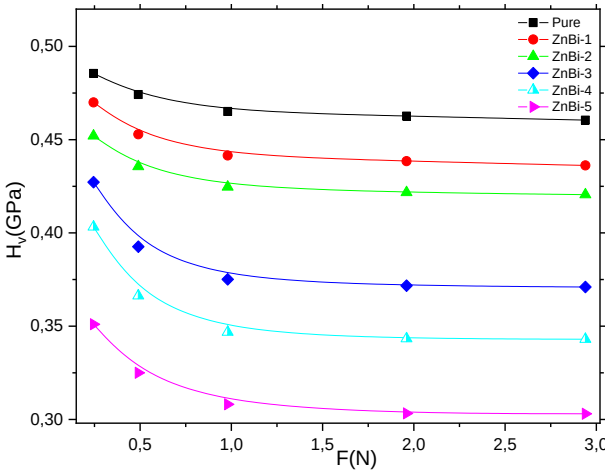


**Fig. 1. Graphs showing the relationship between Vickers $H_v$ parameters and external forces for ZnO-added Bi-2223 ceramic structures.**

Hence, in the current work the optimum results for the mechanical performance are seen in the pure sample. In this respect, the pure ceramic structure possesses the biggest elastic recovery, highest durable tetragonal phase, and the most stabile structure depending on reducing crystallinity issues including stress raisers, lattice strain, and crack initiation regions. This delays dislocation and crack propagation even under higher loads. However, the presence and increase of ZnO addition levels result in increased crystallinity problems, causing mechanical performance deterioration due to stress-induced phase transformations. Numerically, the pure compound exhibits the highest hardness value, peaking at 0.4855 GPa under a 0.295 N load and gradually decreasing under higher loads toward the $H_v$ value of 0.605 GPa (at 2.940 N). In contrast, ZnBi-5 shows the lowest $H_v$ values, reflecting the increased vulnerability to fracture damages.

As for the effect of ZnO semiconductor material on the ISE mechanical behavior for the Bi-2223 ceramics, every compound presents a characteristic ISE behavior. However, the ISE effect degrades with semiconducting addition mechanism, falling the minimum level at x=0.12. On this basis, the pure ceramic material displays the highest ISE behavior whereas the minimum ISE feature is observed for the ZnBi5 ceramic compound. Moreover, the ISE nature helps explain the response of a ceramic structure to applied loads. The pure production process significantly reduces sensitivity to force, improving mechanical performance as much as possible. Figure 1 shows a rapid, nonlinear drop in $H_v$ values as applied loads increase up to about 2.00 N, followed by stabilization at higher loads. This plateau suggests that deformation becomes constrained due to the saturation of slip systems or resistance to stress amplification. The pure sample resists further deformation better at higher loads, reflecting greater crystallinity and mechanical stability.

### 3.2.Role of ZnO semiconductor addition on mechanical characteristics in PL regions

This chapter demonstrates the practical use of theoretical models to analyze the fundamental mechanical properties and load-independent Hv results in the PL regions of ZnO-added Bi-2223 samples in the PL regions using six semi-empirical models (HK, IIC, ML, PSR, EPD, and MPSR) to define the most suitable technique to evaluate the mechanical toughness, strength, and mechanical characteristic behavior. By comparing the models studied, the work provides insights into load-

independent hardness behavior and mechanical performance, improving the understanding of advanced ceramics. The following sections will analyze each model, starting with the ML approach, to explore how addition mechanism affects mechanical properties including strength, stress values, elastic recovery, and phase stability.

### 3.2.1. Investigation of mechanical characteristics of ZnO-added Bi-2223 structures with ML mechanical model

In the present work, we use Meyer's Law to analyze both load-independent and load-dependent $H_v$ regions in ZnO semiconductor impurity ions added Bi-2223 ceramics, assessing mechanical behaviors of ISE or RISE. In this model, the Meyer coefficient (presented as n), derived from the relationship between external loads applied and indentation depth sizes, indicates the material mechanical response (Altunpak, & Ülgen, 2023).

$$F = A_{Meyer} d^{n} \quad (2)$$

In the equation, n>2 points out RISE behavior, n<2 reveals ISE, and n=2 indicates load-independent hardness. In Table 1, it is seen that all n values calculated for ZnO-added Bi-2223 ceramics are below 2, confirming the typical ISE behavior where both elastic and plastic deformations (elastic recovery behavior) are present.

The n values are found to generally decrease with increasing ZnO semiconductor impurity ions due to the new induced crystallinity problems, crack initiation regions, deformations, distortions, lattice strains, impurity residues, chemical bonding, grain mis/alignment, stress

raisers for cracks, microvoids, intergranular interactions, and layer interaction faults in the Bi-2223 system. Thus, the presence and increase in the ZnO impurity damage significantly the crystal quality, force barriers, and active slip systems through the crystal system, encouraging the stress-induced phase transformations in the active layers. The rapid degradation in the values of $H_v$ parameters can be seen in Fig. 2. Especially, the ZnBi5 sample shows the weakest mechanical performance because of a shift from the durable tetragonal phase to a stress-induced phase. Numerically, the pure sample has the largest n value of 1.959, following a considerable decrease in the values depending on the ZnO addition levels.

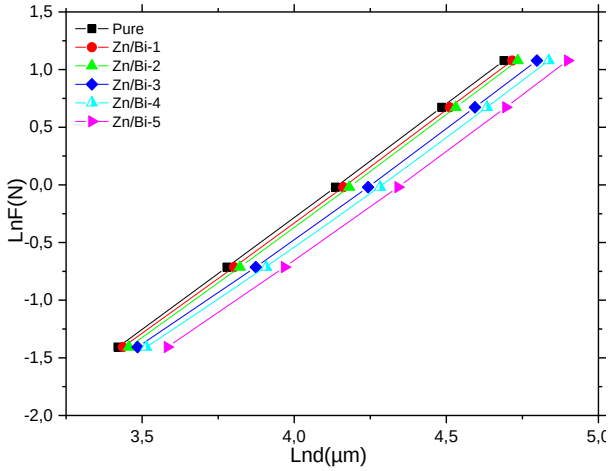


**Fig. 2 Differentiation of lnF against lnd in ZnO-added Bi-2223 ceramic samples.**

The $A_{Meyer}$ values, which are positive across samples, further confirm the typical ISE characteristics. All the samples have the $A_{Meyer}$ values ranging from $2.764\times10^{-4}N/\mu m^2$ to $3.2302.764\times10^{-4}N/\mu m^2$ based on the ZnO addition levels. On this basis, the ZnBi5 ceramic structure

exhibits the minimum value of $2.764\times10^{-4}N/\mu m^2$. The ML model reveals that the pure sample and other Bi-2223 added with very little Zn O addition have superior resistance to external loads and deformations under applied loads due to enhanced performance indicators and phase stability, while ZnBi5 is most sensitive to external stress. Overall, the model effectively demonstrates the mechanical properties of ZnO semiconductor impurity ions added Bi-2223 ceramics.

### 3.2.2. Variation of mechanical characteristics pertaining to ZnO-added Bi-2223 ceramics according to EPD mechanical examination technique

The EPD mechanical investigation model evaluates the mechanical performances as well as durability, structural integrity, sensitivity to applied forces, microhardness properties and load-independent $H_v$ values. In the model calculation, a new term for the irreversible deformation constant ($d_p$) is introduced in the calculations, emphasizing the relationship between recovery mechanisms and indentation depths. The model analyzes how ceramics respond to mechanical forces, distinguishing between elastic and permanent plastic deformations (Ozkurt, 2014).

$$F = A_{EPD}(d_e + d_p)^2 \quad (3)$$

The formula is defined using the extrapolated values from plots of external loads ($F^{1/2}$) and the average depths ($d_p$), as illustrated in Fig. 3.

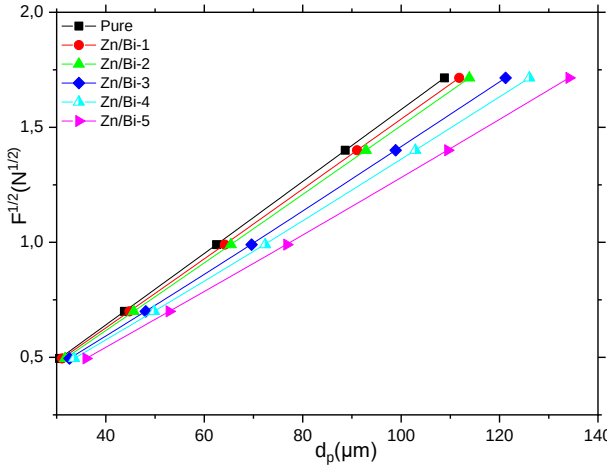


**Fig. 3 Change in $F^{1/2}$ over $d_p$ of all the ZnO-added Bi-2223 materials.**

The coefficient ($d_e$) determines the mechanical behavior (ISE or RISE) under applied loads. All computed values are summarized in Table 1, indicating that ZnO-added ceramics exhibit positive $d_e$ parameters. This confirms that all the prepare structures have the typical ISE behavior. The results show that the ceramics undergo both elastic and plastic deformation, thus indicating that the dominant elastic recovery occurs upon removal of the applied force on the system. Numerically, the pure sample presents the minimum $d_e$ value of $0.169\times10^{-1}$ µm, following a significant increase in the values based on the ZnO addition levels. In this content, the Bi-2223 ceramic structures added with high Zn additions possess the relatively higher $d_e$ value due to their considerable sensitivity to the applied loads.

Regarding $A_{EPD}$ values, the pure ceramic structure shows the highest $0.156\times10^{-1}N^{1/2}/\mu m$, while other samples (especially ZnBi5 sample) exhibit lower values. The

decrease correlates with new induced crystallinity problems, crack initiation regions, deformations, distortions, lattice strains, impurity residues, chemical bonding, grain mis/alignment, stress raisers for cracks, microvoids, intergranular interactions, and layer interaction faults, with the ZnBi5 sample showing the lowest $A_{EPD}$ value of $0.124\times10^{-1}N^{1/2}/\mu m$. This indicates that the inner (pure) ceramic sustains less damage from applied loads, whereas the latter (ZnBi5) sample suffers more severe crack propagation under lower test loads. Correspondingly, the pure structure is the least sensitive to applied forces, ın contrast, the ZnBi5 compound shows the highest sensitivity due to structural issues.

$$H_{EPD} = 1854.4 A_{EPD} \quad (4)$$

The EPD model also analyzes load-independent $H_v$ values for all samples by using the Eq. 4. It is found that the Vickers $H_v$ values in the PL regions are a few lower than expected ones (Table 2). While the EPD model effectively assesses mechanical performance and durability, it is less accurate in determining load-independent $H_v$ values.

**Table 1. Load-dependent $H_v$ values determined by HK, IIC, ML, PSR, EPD, and MPSR mechanical models for ZnO-added Bi-2223 ceramic structures**

| *Samples* | Meyer's Law | | PSR Model | | MPSR Model | | | EPD Model | | HK Model | | IIC Model | |
|---|---|---|---|---|---|---|---|---|---|---|---|---|---|
| | $A_{MEYER}$ x$10^{-4}$ (N/µm²) | n | α x$10^{-4}$(N/µm) | β x$10^{-4}$ (N/µm²) | W x$10^{-2}$ (N) | $A_{0MPSR}$ x$10^{-3}$ (N/µm) | $A_{1PSR}$ x$10^{-4}$ (N/µm²) | $d_e$ x$10^{-1}$ (µm) | $A_{2EPD}$ x$10^{-1}$ ($N^{1/2}$/µm) | W x$10^{-1}$ (N) | $A_{3HK}$ x$10^{-4}$ (N/µm²) | K x$10^{-2}$ ($N^{(3-5mA)/3}$/ $µm^{(2-3m)}$) | m |
| ***Pure*** | 2.994 | 1.959 | 5.392 | 2.432 | 0.845 | 2.234 | 2.456 | 0.169 | 0.156 | 0.151 | 2.472 | 7.217 | -0.151 |
| ***Zn/Bi-1*** | 3.050 | 1.943 | 7.108 | 2.286 | 1.653 | 1.064 | 2.330 | 0.228 | 0.151 | 0.198 | 2.337 | 2.697 | -0.225 |
| ***Zn/Bi-2*** | 2.923 | 1.945 | 6.687 | 2.204 | 2.376 | -1.774 | 2.265 | 0.219 | 0.149 | 0.183 | 2.253 | 2.837 | -0.217 |
| ***Zn/Bi-3*** | 3.230 | 1.896 | 11.300 | 1.895 | 5.989 | -9.182 | 2.036 | 0.388 | 0.138 | 0.299 | 1.977 | 0.141 | -0.441 |
| ***Zn/Bi-4*** | 3.215 | 1.881 | 12.400 | 1.737 | 7.198 | -11.300 | 1.894 | 0.442 | 0.132 | 0.337 | 1.825 | 0.072 | -0.484 |
| ***Zn/Bi-5*** | 2.764 | 1.889 | 11.400 | 1.539 | 10.142 | -6.860 | 1.651 | 0.431 | 0.124 | 0.345 | 1.612 | 0.027 | -0.543 |

**Table 2. Load-independent $H_v$ parameters in the PL regions based by HK, IIC, PSR, EPD, and MPSR mechanical models.**

| *Samples* | $H_{PSR}$ *(GPa)* | $H_{MPSR}$ *(GPa)* | $H_{EPD}$ *(GPa)* | $H_{HK}$ *(GPa)* | $H_{IIC}$ *(GPa)* | *Hv (GPa)* |
|---|---|---|---|---|---|---|
| ***Pure*** | 0.451 | 0.455 | 0.451 | 0.458 | 0.472 | 0.461-0.486 |
| ***Zn/Bi-1*** | 0.424 | 0.432 | 0.424 | 0.433 | 0.450 | 0.436-0.470 |
| ***Zn/Bi-2*** | 0.409 | 0.421 | 0.409 | 0.418 | 0.434 | 0.420-0.452 |
| ***Zn/Bi-3*** | 0.351 | 0.377 | 0.352 | 0.367 | 0.385 | 0.371-0.427 |
| ***Zn/Bi-4*** | 0.322 | 0.351 | 0.323 | 0.338 | 0.361 | 0.343-0.403 |
| ***Zn/Bi-5*** | 0.285 | 0.306 | 0.286 | 0.298 | 0.317 | 0.303-0.389 |

### 3.2.3. Research of mechanical characteristics of ZnO-added Bi-2223 ceramic structures with HK approach

The HK mechanical characterization model is well-regarded for assessing critical performance indicators, flexibility, elastic recovery mechanisms, the stabilization of the tetragonal phase, structural integrity, resistance to external loads, stress amplification sites, and load-independent $H_v$ values of ceramics in the PL regions. The model incorporates a constant, denoted as W, that relates the applied load to elastic and plastic deformation. The effective load term correlates the test load with the resulting irreversible deformation, represented mathematically as follows:

$$F - W = A_{HK} d^2 \quad (5)$$

In this equation, the $A_{HK}$ constant for the ZnO-added materials is determined through extrapolations based on the relationship between the square root of the applied test loads ($F^2$) and the notch depth lengths ($d^2$), as shown in Fig. 4. The resulting parameters are detailed in Table 1, indicating that every material produced exhibits positive W values (changing from $0.151 \times 10^{-1}$ N for the pure material to $0.345 \times 10^{-1}$ N for ZnBi5 sample), supporting typical ISE behavior. This suggests a combination of reversible and irreversible deformations under applied loads. Besides, it is interesting that with the increase in the ZnO semiconductor addition level, the decrement trend in the values of W parameters stems from both the increase in the systematic faults (crystallinity problems, crack initiation regions, deformations, distortions, lattice strains, impurity residues,

chemical bonding, grain mis/alignment, stress raisers for cracks, microvoids, intergranular interactions, and layer interaction faults) and the decrease in the crystal quality, force barriers, and active slip systems in the crystal structure. The W parameter clearly indicates that the presence and increase in the ZnO impurity ions harm the durable tetragonal phase.

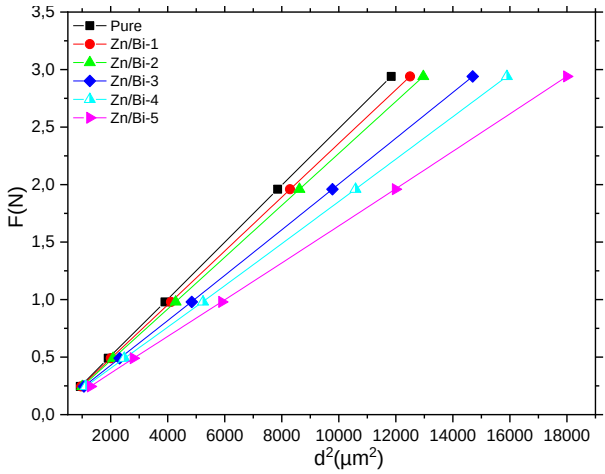


**Fig. 4. Plots between F and $d^2$ for every material studied.**

Similarly, the $A_{HK}$ coefficients exhibit the similar behavior with the impurity ions. Namely, there is a considerable decrease in the values of $A_{HK}$ parameter changing from $2.472 \times 10^{-4}$ N/μm² (for the pure sample) to 1.612 N/μm² (for the ZnBi5 sample). Hence, the ZnBi5 structure is the most responsive to the applied test loads.

The HK model also evaluates load-independent Hv values in the PL regions using the following formula:

$$H_{HK} = 1854.4 A_{HK} \quad (6)$$

The computed $H_{HK}$ values are numerically presented in Table 2. The load-independent $H_v$ values

obtained are found to be closer to the actual values compared to those calculated by other models. However, the HK approach does not fully capture the original Vickers $H_v$ parameters in the PL regions. Regardless, the HK mechanical model effectively evaluates the mechanical performance quantities, phase stability, and mechanical characteristics of ZnO semiconductor added ceramics. Although the model calculations are less effective in examining the load-independent $H_v$ microhardness in the PL regions, it provides a superior method to evaluate the real $H_v$ parameters compared to other theoretical mechanical computation techniques.

#### 3.2.4. Inspection of general mechanical performance quantities and mechanical characteristics of ZnO-added Bi-2223 materials with IIC model

The IIC mechanical model is used to evaluate the mechanical performance, stability of the durability of tetragonal phase, mechanical characteristics, and load-independent $H_v$ properties of ZnO-added advanced ceramic compounds. The model comprises four key components: i) notch friction, ii) elastic deformation, iii) irreversible deformation, and iv) crack formations. The components mentioned arise from the resistance the material surfaces during indentation process along the diagonal depths (Hays, & Kendall, 1973; Akkurt, & Yildirim, 2016; Li, & Bradt, 1996). The IIC model calculates load-independent $H_v$ values using the following equation:

$$H_{IIC} = \lambda_1 K_1 \left(F/d^2\right) + K_2 \left(F^{5/3}/d^3\right) \quad (7)$$

In this equation, $\lambda_1$ is a material-specific constant, $K_1$ relates to the indenter geometry, and $K_2$ is determined based on external loads. For perfectly plastic materials ($\lambda_1 = 1$), $K_2$ becomes zero, simplifying the equation to $K_1 (F/d^2)$. In contrast, for perfectly brittle materials ($\lambda_1 = 0$), only $K_2$ remains. Since ceramics are brittle, the equation simplifies to:

$$H_{IIC} = K\left(\frac{F^{5/3}}{d^3}\right)^m \quad (8)$$

Constants k and m in the formulation represent load-independent $H_v$ values, derived from graphs plotting $\ln(H_v)$ against $\ln(F^{5/3}/d^3)$, as illustrated in Fig. 5. The k and m coefficients calculated for all ceramic structures are presented in Table 1. In the IIC model, the critical value m = 0.6 indicates the material behavior: if $m < 0.6$, the material shows typical ISE behavior; if $m > 0.6$, it exhibits unusual RISE behavior. Table 1 shows that all ZnO-added compounds have m values below 0.6, confirming ISE behavior, albeit with varying trends. Numerically, m value is observed to be about -0.151 for the pure sample, -0.225 for the ZnBi1, -0.217 for the ZnBi2, -0.441 for the ZnBi3, -0.484 for the ZnBi4, and -0.543 for the ZnBi5 compound. Shortly, at higher substitution levels, significant decreases in m occur due to severe microscopic crystal structure issues, increased deformations, crack initiation regions, distortions, lattice strains, impurity residues, chemical bonding, grain misalignment, stress raisers for cracks, microvoids, intergranular interactions, and layer interaction faults. Moreover, K values are found to change from $7.217 \times 10^{-2}$ ($N^{(3-5mA)/3}/\mu m^{(2-3m)}$) for the pure material to

$0.027x10^{-2}$ ($N^{(3-5mA)/3}/\mu m^{(2-3m)}$) for the ZnBi5 compound. This decrement shows that the sensitivity to applied loads increases depending on the ZnO semiconductor addition levels.

Additionally, the IIC model allows for the evaluation of load-independent $H_v$ values for Bi-2223 samples with ZnO additions. It is observed that the calculated $H_v$ parameters presented in Table 2 align closely with actual $H_v$ values across all load regions. Consequently, among the models used in this study, the IIC model proves to be the most effective for assessing mechanical performance, tetragonal phase stabilization, and load-independent $H_v$ values in the PL regions of the ZnO-added Bi-2223 ceramics.

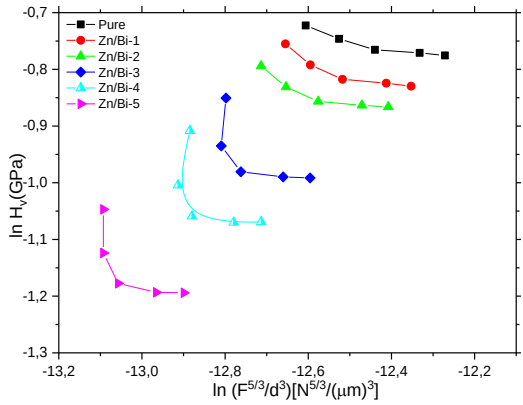


**Fig. 5 Change of ln($H_v$) versus ln($F^{5/3}/d^3$) belonging to ZnO-added Bi-2223 ceramic structures.**

### 3.2.5. Mechanical characteristic features of ZnO-added Bi-2223 structures with respect to PSR model

The PSR model is known to be effective for evaluating both load-dependent and load-independent $H_v$

parameters in ceramic composites and addresses the energy distribution among microscopic crystallinity issues. The model integrates the surface energy (α) with $H_v$ constants to determine the mechanical characteristic behavior. While the surface energy indicates the overall mechanical properties, the microhardness (β) reflects the resistance to deformation. α and β together distinguish between ISE and RISE behavior in ceramics (Erdem, Zalaoglu, Ulgen, Turgay, & Yildirim, 2021).

$$F = \alpha d + \beta d^2 \tag{9}$$

The α and β parameters in the PSR model are derived from Eq. 9. Figure 6 illustrates the relationship between applied test loads (F/d) and mean notch diagonal length (d) for every compound prepared in the present work. It is observed that the addition of ZnO semiconductor impurity significantly alters the curves, indicating changes in critical performance indicators, elastic recovery mechanisms, tetragonal phase stabilization, structural integrity, and resistance to external loads.

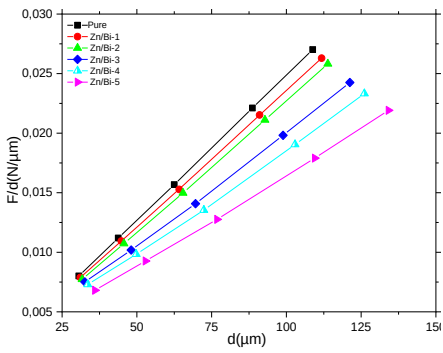


**Fig. 6 Hardness plots between F/d and d of all the ZnO-added Bi-2223 ceramic systems**

Table 1 lists the numerical values of α and β parameters. All α values (in the positive regions) indicate typical ISE behavior. In the table, the value is observed to be about $5.392\times10^{-4}$ N/μm foe the pure Bi-2223 sample, following the increasing trend depending on the ZnO impurity additions because of the significant degradation in the crystallinity, performance indicators, and intergranular interactions. The β parameter, linked to resistance against deformation, decreases from $2.432\times10^{-4}$ N/μm$^2$ for the pure sample to $1.539\times10^{-4}$ N/μm$^2$ for the ZnBi5 ceramic structure. The decrement trend results from the degradation of mechanical strength and durability depending on the increase in the systematic faults. The combination of α and β parameters reveals that the pure Bi-2223 ceramic possesses the highest crystal quality, tetragonal phase stability, and the slowest dislocation and crack propagations along the crystal system. Thus, the model is successful to determine the change in the general mechanical quantities with the ZnO semiconductor impurity ions.

$$H_{PSR} = 1854.4\beta \tag{10}$$

The calculated $H_{PSR}$ values in Table 2 also show that load-independent $H_v$ values in the PL regions are significantly lower than actual $H_v$ values. In summary, the PSR model is effective for evaluating load-dependent mechanical properties and related variations but is less reliable for predicting accurate load-independent $H_v$ values in the PL regions.

### 3.2.6. Inspection of mechanical performance and characteristics of ZnO-added Bi-2223 ceramics in terms of MPSR

The MPSR mechanical investigation method has been widely used to evaluate the mechanical performance, properties and load-independent Hv values in the PL regions of specimens. The model is based on the minimum indentation load ($W_{MPSR}$), which is related to the diagonal depth of the indentation on the material surface and indicates the load required to initiate plastic deformation (Gong, Wu, & Guan, 1999). This parameter is crucial for understanding the elastic recovery mechanism and the main characteristics of ceramic compounds.

$$F = W_{MPSR} + A_{0MPSR}d + A_{1MPSR}d^2 \quad (11)$$

The MPSR formula given in Eq. 11 incorporates constants $A_{0MPSR}$ and $A_{1MPSR}$, which account for energy loss due to crystallinity problems, crack initiation regions, deformations, distortions, lattice strains, impurity residues, chemical bonding, grain mis/alignment, stress raisers for cracks, microvoids, intergranular interactions, and layer interaction faults in the Bi-2223 system. Figure 7 illustrates the relationship between applied loads (F) and average notch depths (d) for the ZnO-added Bi-2223 ceramic structures. The numerical values for $W_{MPSR}$, $A_{0MPSR}$, and $A_{1MPSR}$, derived from extrapolation methods, are detailed in Table 1. The results calculated display that the ZnO impurity addition significantly affects the performance indicators, mechanical strength, elastic recovery mechanisms, and stabilization of tetragonal phase. In the calculations, a positive $W_{MPSR}$ value indicates typical ISE

behavior, while a negative value indicates unusual RISE behavior. Table 1 confirms that all ceramic samples exhibit positive $W_{MPSR}$ values ranging from 0.845N to 10.140 N, indicating dominant elastic recovery mechanisms. It is apparent that there is a systematic decrement in the $W_{MPSR}$ values because of the suppression in the crystallinity quality based on the rapid increase in the systematic faults, force barriers, and especially active slip systems in the crystal structure.

The $W_{MPSR}$ parameter shows the degradation in the mechanical performance quantities, recovery mechanisms, stabilization of tetragonal phase, mechanical strength, durability, elastic recovery mechanisms, tetragonal phase stabilization, structural integrity, and resistance to external loads. Moreover, $A_{1MPSR}$ values reflect variations in mechanical performance. For example, the pure sample has the highest $A_{1MPSR}$ value of approximately $2.456\times10^{-4}$ N/μm$^2$, following a regular decrease toward the global minimum value of $1.651\times10^{-4}$ N/μm$^2$ at the highest addition level (x = 0.12). The changes indicate degradations in the stabilization of the tetragonal phase, mechanical strength, and resilience to external loads.

$$H_{MPSR} = 1854.4A_{1MPSR} \quad (12)$$

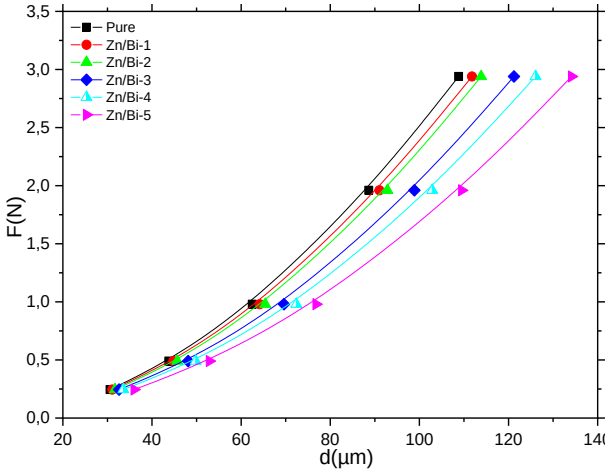


**Fig. 7. Change of F as a function of d for all the materials studied.**

Additionally, the MPSR model allows for the evaluation of load-independent $H_v$ values for Bi-2223 samples with ZnO semiconductor impurity additions. The calculated $H_v$ parameters presented in Table 2, are substantially higher than the original Vickers $H_v$ values across all the applied test loads, particularly at higher loads, due to increased granularity in the crystal structure. Overall, the MPSR mechanical calculation model effectively assesses the mechanical performance, durability, tetragonal phase stabilization, and mechanical properties of ZnO-added Bi-2223 ceramic structures but is limited in analyzing load-independent $H_v$ parameters in the PL regions.

## 4. CONCLUSION

This study investigates the effects of different ZnO semiconductor addition levels on the mechanical performance, elastic recovery mechanisms, mechanical strength, durability tetragonal phase stabilization, structural integrity, and resistance to external loads of Bi-2223 structures using a rigorous approach involving several mechanical computation models (HK, IIC, ML, PSR, EPD, and MPSR). The analysis covers key mechanical performance aspects such as critical stress, deformation behavior, phase stability, and load-independent microhardness ($H_v$) parameters. The results show that the mechanical characteristic properties of ZnO-added Bi-2223 ceramics degrade significantly with increasing ZnO semiconductor impurity ions. The suppression trend stems from the new induced crystallinity problems, crack initiation regions, deformations, distortions, lattice strains, impurity residues, grain mis/alignment, stress raisers for cracks, microvoids, intergranular interactions, and layer interaction faults in the Bi-2223 system. Correspondingly, the presence and increase in the ZnO impurity significantly harm the crystal quality, force barriers, and active slip systems through the crystal system. Namely, the ZnO causes the revival of the stress-induced phase transformations in the active layers. The selected models in the literature provide detailed insights into the mechanical strength, durability, and resistance to external stresses of the ZnO-added Bi-2223 systems under applied loads. Notably, the IIC mechanical approach is found to confirm particularly effective in describing elastic and plastic deformations and accurately assessing load-independent

$H_v$ data in the PL regions. We also find strong consistency among various models, highlighting the strength of the mechanical performance analysis. The research advances the understanding of ZnO-added Bi-2223 ceramics and provides a solid foundation for future exploration of the mechanical behavior of ceramic structures, making significant contributions to ceramic materials science. Overall, the modeling approach guides technological progress in mechanical analysis and materials development.

## REFERENCES

Akkurt, B., & Yildirim, G. (2016). Change of mechanical performance and characterization with replacement of Ca by Gd nanoparticles in Bi-2212 system and suppression of durable tetragonal phase by Gd. Journal of Materials Science: Materials in Electronics, 27, 13034-13043.

Altunpak, Y., & Akbulut, H. (2009). Effects of aging heat treatment on machinability of alumina short fiber reinforced LM 13 aluminum alloy. The International Journal of Advanced Manufacturing Technology, 43, 449-454.

Altunpak, Y., & Akbulut, H. (2017). Mechanical properties of a squeeze-cast 2124 Al composite reinforced with alumina short fibre. Metallurgical Research & Technology, 114(5), 509.

Altunpak, Y., Aslan, S., Guler, M.O., & Akbulut, H., (2016). Effect of alternative heat-treatment parameters on the aging behavior of short-fiber-reinforced 2124 Al composites, Materiali in Tehnologije, 50, 1011-1016.

Altunpak, Y., & Ülgen, A.T. (2023). Change of microstructural, crystalline quality, and surface morphological features of $Bi_{2.1}Sr_{2.0}Ca_{2.1}Cu_{3.0}O_y$ ceramic materials with the CdO addition, 21-44.

Ateş, A. (2013). The Effect of Polymer-Cement Stabilization on the Unconfined Compressive Strength of Liquefiable Soils. International Journal of Polymer Science, 2013(1), 356214.

Ateş, A. (2016). Mechanical properties of sandy soils reinforced with cement and randomly distributed glass fibers (GRC). Composites Part B: Engineering, 96, 295-304.

Erdem, U., Zalaoglu, Y., Ulgen, A. T., Turgay, T., & Yildirim, G. (2021). Role of trivalent Bi/Tm partial substitution on active operable slip systems in Bi-2212 crystal structure. *Cryogenics*, *113*, 103212.

Erden, M. A., Tasliyan, M. F., & Akgul, Y. (2021). Effect of TiC, TiN, and TiCN on microstructural, mechanical and tribological Properties of PM steels. Science of Sintering, 53(4), 497-508.

Gong, J., Wu, J., & Guan, Z. (1999). Examination of the indentation size effect in low-load Vickers hardness testing of ceramics. Journal of the European Ceramic Society, 19(15), 2625-2631.

Haskul, M., Ülgen, A. T., & Döner, A. (2020). Fabrication and characterization of Ni modified $TiO_2$ electrode as anode material for direct methanol fuel cell. International Journal of Hydrogen Energy, 45(7), 4860–4874.

Haskul, M. (2020). Elastic state of functionally graded curved beam on the plane stress state subject to thermal load. Mechanics Based Design of Structures and Machines, 48(6), 739–754.

Haskul, M., & Kisa, M. (2021). Free-vibration analysis of cracked beam with constant width and linearly varying thickness, Emerging Materials Research, 11(1), 125–137.

Hays, C., & Kendall, E.G., (1973). Metallography 6, 275–366.

Hilgenkamp, H., & Mannhart, J. (2002). Grain boundaries in high-$T_c$ superconductors. Reviews of Modern Physics, 74(2), 485.

Li, H., & Bradt, R. C. (1996). The effect of indentation-induced cracking on the apparent microhardness. Journal of materials science, 31, 1065-1070.

Li, H., & Bradt, R.C., (1993). The microhardness indentation load/size effect in rutile and cassiterite single crystals, J. Mater. Sci. 28, 917-926.

Michels, B. D., & Frischat, G. H. (1982). Microhardness of chalcogenide glasses of the system Se-Ge-As. Journal of Materials Science, 17, 329-334.

Oh, S. Y., Kim, H. R., Jeong, Y. H., Hyun, O. B., & Kim, C. J. (2007). Joining of Bi-2212 High-$T_c$ superconductors and metals using indium solders. Physica C: Superconductivity and its applications, 463, 464–467.

Ozkurt, B., (2014). The Influence of Na addition on the mechanical properties of Bi-2212 superconductors, J. Supercond. Nov. Magn. 27, 2407–2414.

Plakida, N. (2010). High Temperature Cuprate Superconductors. Springer Series in Solid-State Sciences. Springer. p. 480. ISBN 9783642126321.

Pul, M. (2018). Effect of B4C reinforcement ratio and sintering temperature on the mechanical behavior in Al-B4C composites. Science of Sintering, 50(1), 51-61.

Sangwal, K. (2000). On the reverse indentation size effect and microhardness measurement of solids. Materials Chemistry and Physics, 63(2), 145-152.

Sheahen, T.P. (2002). Introduction to High-temperature Superconductivity, 1st ed., Kluwer Academic Publishers, New York, Boston.

Tarkanian, M. L., Neumann, J. P., & Raymond, L. (1973). The science of hardness testing and its research application. Metal Park, Ohio:(American Society for Metals.

Yamauchi, H., & Karppinen, M. (2000). Application of high-pressure techniques: stabilization and oxidation-state control of novel superconductive and related multi-layered copper oxides. Superconductor Science and Technology, 13(4), R33.

Yaşar, M., & Altunpak, Y. (2009). The effect of aging heat treatment on the sliding wear behaviour of Cu–Al–Fe alloys. Materials & Design, 30(3), 878-884.

# ALBEDO PROPERTIES OF SOME SELECTED THERMOLUMINESCENT DOSIMETRIC COMPOUNDS

**Ahmet TURŞUCU**[1]

## 1. INTRODUCTION

Electromagnetic radiation, essential in today's technology, is defined as non-ionizing radiation if it has enough energy to vibrate or move the atoms in a molecule. Non-ionizing radiation is used daily, from heating a meal to transmitting television broadcasts. Since it has a very low-frequency value, its frequency range extends from audible electromagnetic radiation to ultraviolet frequency in the visible region. Unlike this type of radiation, the energy of ionizing radiation is sufficient to break chemical bonds. For example, x-rays and gamma rays have very high frequencies ($f > 10^{19}$ Hz) and short wavelengths ($< 10^{-8}$ meters) at the upper end of the spectrum. The types of radiation in the mentioned range have a very high energy level.

Along with the development of radiation dosimetry due to the use of radiation for medical and therapeutic purposes, the tools used to make accurate dose measurements have also developed. At the same time, theoretical methods have been designed to make dose measurements and calculations more precise and reliable.

[1] Assoc. Prof., Şırnak University, Engineering Faculty, Electric-Electronic Engineering Dep., ahmettursucu@sirnak.edu.tr, ORCID: 0000-0002-4963-697X.

As it is known, in radiation therapy applications, diseased organs are exposed to radiation at high doses. The applied radiation dose is an essential factor affecting the success rate of the treatment. For this reason, the radiation to be applied to the tumor must be applied sensitively. Therefore, the calibration of the radiation to be used and the correct calculation of the application dose is required.

Thermoluminescent dosimetric materials protect against the harmful effects of radiation, radiation therapy, space applications, and many different fields of technology by reporting high or low doses of radiation. To achieve this, these materials are used as active ingredients in radiation measuring devices. Thermoluminescent dosimetric materials are expected to be continuously producible, have high hygroscopicity, show high sensitivity to radiation at very low doses, or respond well to very high radiation levels. For this purpose, LiF (8.3), whose effective atomic number is very close to water and living tissue, is widely used in radiotherapy. Lithium tetraborate is more tissue equivalent than LiF. However, LiF is inherently molten as it absorbs high atmospheric moisture at room temperature, causing the signals it stores to disappear quickly. However, lithium tetraborate is inherently molten as it absorbs high atmospheric humidity at room temperature and generates the signals it stores to disappear soon. The very close tissue effective atomic number of lithium tetraborate (7.3) outweighs the disadvantage and is only valuable for X-ray uses. Although calcium sulfate is far from being a tissue equivalent with its effective atomic number of 15.6, it is pretty close to the effective atomic number of bone with this effective atomic number. Due to its susceptible structure, it

can be used in protection dosimetry. It is vulnerable and, therefore, can be used for protection dosimetry. Similarly, calcium fluoride is also used in protection dosimetry with its effective atomic number of 16.9 and susceptible structure. The thermoluminescent dosimetric compounds used in this study are given in Table 1.

**Table 1. Thermoluminescent Dosimetric compounds used in experiments.**

**Thermoluminescent Dosimetric Compounds**

| Number | Compound | Pellet ($gr/cm^2$) | Effective Atomic Number |
|---|---|---|---|
| 1 | $MgSO_4$ | 0.19974 | 16.64481 |
| 2 | $CdSO_4$ | 0.35386 | 31.17127 |
| 3 | $Al_2O_3$ | 0.19918 | 15.12184 |
| 4 | $MnSO_4$ | 0.37948 | 19.61667 |
| 5 | $ZnSO_4$ | 0.33772 | 17.26406 |
| 6 | $CaSO_4$ | 0.26473 | 18.09335 |
| 7 | CaF | 0.40133 | 19.52779 |
| 8 | $NaSO_4$ | 0.34355 | 17.26406 |
| 9 | $H_2Fe_4O_{22}S_5$ | 0.23106 | 18.10585 |
| 10 | $Ca_5(SO_4)_3$ | 0.10027 | 17.61290 |
| 11 | $SiO_2$ | 0.21842 | 17.05867 |
| 12 | $CaCO_3$ | 0.22449 | 18.32658 |
| 13 | $BaSO_4$ | 0.31180 | 29.06528 |

It is widely practiced to determine protective parameters and to use these values in dosimetric studies to protect employees and patients from the harmful effects of radiation. [1, 2, 3, 4, 5, 6, 7, 8, 9, 10, 11, 12]. Among the mentioned shielding parameters is the determination of albedo values. Albedo measures the scattering of characteristic X-rays directed on the material used for analysis. The albedo values obtained from the different scattering values obtained include three subcomponents.

The literature has included albedo numbers, energy levels, and doses. Numerous researchers have studied this subject, and many articles in this field are in the literature [13, 14, 15, 16, 17, 18, 19, 20].

The purpose of this article is related to reporting the reactions of TLD materials, which are frequently used in clinical and industrial areas, to radiation tests. The main reasons why the materials we constantly talk about as TLD are gaining importance as a field of study are that they are cheap, can be used continuously, are easy to produce, are insensitive to destructive environments such as humidity, and, most importantly, are used in ensuring radiation safety. Thermoluminescent materials are essential in dosimeters and in calculating individual absorbed doses. The sole purpose of this study is to test the usability of these dosimetric materials as shielding products. In this study, the albedo factor, one of the radiation shielding parameters, is focused. The mentioned parameter includes different measurements and calculations made on thermoluminescent dosimetric materials. By examining the behaviour of thermoluminescent materials commonly used in personal dosimeters against radiation, dosimeters that provide more efficient and accurate results can be designed and produced. Based on the necessity of conducting a study on this subject, the necessary calculations were made after preparing the existing experimental setup and presenting the results in graphs.

## 2. MATERIALS AND METHODS

### 2.1.Albedo Parameters

Albedo is the rate of the intensity of the primary photons incident to the face and the intensity of the photons scattered from the face. It gives information about the reflectivity (property) of the face. In addition to a scattering of photons from the face, there is also scattering in the sample [13]. Photon reflection decreases with the viscosity and the infinitesimal number of the sample. As the infinitesimal number increases, the probability of photoelectric immersion increases, and therefore, the probability of multiple scattering diminishes. Suppose the energy of the incident photon is small. In that case, the photons access lower into the sample, and the probability of photons being backscattered out of the sample increases, hence the albedo. Albedo is a pivotal parameter extensively used in land face energy balance studies, medium and long-term rainfall vaticinations, and climate change exploration on a global scale [14]. It is the rate of the reflected radiation from the face to the incident radiation. Albedo is one of the primary motorists of energy balance and the commerce between the land face and the atmosphere, as it measures the capacity of a face to reflect solar radiation.

The increase in albedo causes a drop in net radiation, a reduction in latent and sensible heat, and a decaying of low-position confluence. As a result, pall conformation and rush drop. Soil humidity can also drop, adding the face albedo and creating a positive feedback medium. Reduced pall cover causes an increase in solar radiation and further increases the net radiation, causing negative feedback.

Albedo is pivotal in maintaining a stable state [15]. Thus, it is essential to determine the face radiation between positive and negative feedback mechanisms budget and atmospheric action during global and indigenous climate change. Spatial and temporal variations of face albedo are told by natural processes similar to soil humidity, foliage dynamics, snow cover, land use, and other mortal conditioning.

### 2.2.Calculation of Albedo Parameters

An experimental setup was designed in the laboratory to examine the radiation shielding properties of TLD samples. In this setup, a 5 Ci Am-241 source and an HPGe detection system are used in collection of x-rays and evaluation of the characteristic peaks. Calculations were made using the spectroscopic data obtained as a result of the experimental procedures, and albedo parameters were obtained. The calculations made, and the equations used for this purpose are given in detail in the relevant sections.

The sample chamber and experimental setup used in this study, in which albedo parameters were determined, are shown in Figures 1 and 2, respectively. The sample chamber used in the setup minimizes the characteristic peak effect of multiple backscattering and the consequences of scattering on the base counts. In addition, this chamber acted as a protector by ensuring that the researcher was not affected by radiation. The sample chamber, which benefits the counting system and the researcher, is covered with a conical lead collimator. It plays a vital role in obtaining a monochromatic spectrum and minimally affecting it until it reaches the detector. A

computer-controlled counting system controls monochromatic radiations from the sample chamber to the detector. In this counting system, the computer is assisted by a multi-channel analyzer and the Genie-2000 program. Characteristic peaks were obtained with the multi-channel analyzer and Genie-2000 program, and the counts obtained in the peaks were determined by Origin 7.5.

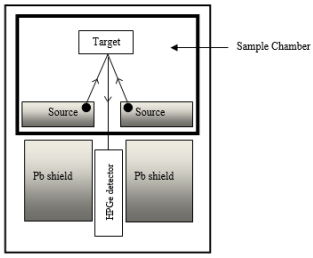


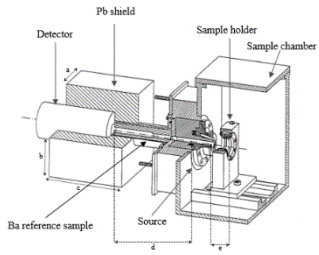


**Figure 1. Experimental setup (radius of collimator is 0.53 cm).**

**(This figure is only a schematic diagram of experimental setup.)**

**Figure 2. Sample chamber (a=6.5 cm, b=6.3 cm, c=13.5 cm, d=11 cm, e=5 cm).**

The area values below the scattering peaks are used to calculate the albedo parameters. The albedo number is the first of the mentioned albedo parameters, calculated as the ratio of the photons reflected from the target material to all photons reaching the target material. Detector efficiency and solid angle values are effective in the calculation. The equation used in the analysis is given below.

$$A_N = \left[\frac{N_{bs}/\varepsilon(E_{bs})}{(N_i/\varepsilon(E_i))(1/d\Omega)(1/2)}\right] \quad (1)$$

The term $\varepsilon(E_{bs})$ and $\varepsilon(E_i)$, used in the formula for calculating the albedo number, represents the photopic efficiency of the detector used in the experiment. The

photopic efficiency of the HPGe detector is calculated using the data obtained from the experimental system of different pure elements ($_{13}$Al, $_{20}$Ca, $_{22}$Ti, $_{23}$V, $_{26}$Fe, $_{28}$Ni, $_{30}$Zn, $_{39}$Y, $_{42}$Mo, $_{45}$Rh, $_{47}$Ag, $_{50}$Sn, $_{57}$La, $_{66}$Dy, $_{70}$Tb, $_{79}$Au, $_{82}$Pb). The terms $N_{bs}$ and $N_i$, used in the formula, refer to the areas under the peaks formed by the backscattered and incident photons, respectively. Also, the solid angle term used in the procedure is expressed by the term $d\Omega$, and the central angle is a steradian with a radius of 1 m and the tip of the cone at the centre of the sphere and equal to the area of 1 m$^2$ seen by the cone on the surface of the sphere. The solid angle unit is steradian, and its symbol is (sr). The steradian is equal to the angle of space that takes the sphere's centre as its apex and divides the area on the sphere's surface by a square equal to the sphere's radius. The factor 1/2 is included in the denominator because half of the gamma photons emitted by the radioactive source fall on the target.

Another albedo parameter, the ratio of the energy of the backscattered photons with the energy of the incoming photons, is used to calculate the albedo energy. The formula for the calculation is given below.

$$A_E = \left[\frac{E_{bs}}{E_i}\right] A_N \qquad (2)$$

In this formula, the previously calculated albedo number is used. In addition, the terms $E_{bs}$ and $E_i$, also used in the equality, express the energies of backscattered and incident photons. Finally, the albedo dose was calculated using the albedo parameters and the data from the experimental study. The formula used in the calculation is given below.

$$A_D = \left[\frac{\sigma_a(E_{bs})}{\sigma_a(E_i)}\right] A_E \quad (3)$$

In this equation, the incident and backscattered photon energies' air absorption coefficients are used and expressed in terms $\sigma_a(E_{bs})$ and $\sigma_a(E_i)$, respectively. The XCOM program was used to calculate the absorption coefficient of the air in the incident and scattered photon energies [16]. In the absorption coefficient of air, since air is not a pure element, the absorption values of all the elements in its content are considered separately. The percentage values of the elements that make up the air are presented in Table 2.

**Table 2. Table of gaseous composition of dry air.**

| Constituent | Chemical symbol | Mole percent |
|---|---|---|
| Nitrogen | $N_2$ | 78.084 |
| Oxygen | $O_2$ | 20.947 |
| Argon | Ar | 0.934 |
| Carbon dioxide | $CO_2$ | 0.0350 |
| Neon | Ne | 0.001818 |
| Helium | He | 0.000524 |
| Methane | $CH_4$ | 0.00017 |
| Krypton | Kr | 0.000114 |
| Hydrogen | $H_2$ | 0.000053 |
| Nitrous oxide | $N_2O$ | 0.000031 |
| Xenon | Xe | 0.0000087 |
| Ozone | $O_3$ | 0.00000001 |

## 3. RESULT AND DISCUSSION

Thermally-induced luminescence (TSL), or simply Thermoluminescence (TL), is the phenomenon of luminescence as a result of thermally induced recombination (recombination) of trapped electrons and holes in a previously irradiated material. Pre-irradiation

occurs by bombarding the material with UV light, X-rays, gamma rays, or energetic electrons. Irradiation generates free electron and hole pairs, many of which are recombined in the material. Still, some electrons and holes are locally trapped in defect centres, such as an impurity or oxygen vacancy defect. If the electron or vacuum trap binding energies are high enough, irradiation to the conduction or valence band, respectively, is not possible at the temperature at which it is made.

For this reason, these load carriers remain in the trap after teleportation. However, if the sample is heated, the recombination probability increases with increasing temperature, resulting in an increased light output with temperature until all traps are emptied [21]. The emission of photons also ends with the end of the traps, and the temperature versus light intensity curve I(T), called the scintillation curve, is obtained. By analyzing the scintillation curve, information such as trap depth and trap concentration can be obtained [22].

Different studies on thermoluminescence kinetics continue to be a current field of study and attract the attention of researchers due to the importance of knowing the trapping values and band structures of TL materials. Clinical applications of the materials discussed in this study are areas of study that should be repeated continuously in order to increase the reliability of the application of x-ray, gamma ray, and proton tests to be performed on the same samples. In clinical applications, tissue equivalent TLD materials must be tested, especially in skin radiation dose assessments. Thanks to the continuously repeated tests, the

incorrectly evaluated behaviours of some such materials are revealed, and the validity of missing or incorrect information is removed. This information is usually the calculation of the angles of arrival and departure of ionizing radiations and the ionization energies of these rays.

This study, similar to the ones described above, includes calculating the data obtained using the scattering values of radioactive rays over compounds with thermoluminescent properties. The radiation shielding properties of the target materials are determined by calculating the scattering data ratio values, also called albedo factor parameters.

The current experimental findings indicate that for each target composed of various elements, the count of multiple backscattered events rises with a higher atomic number. This rise in the number of backscattered photons in relation to changes in atomic number is attributed to the increase in scattering centres available for the primary gamma rays to interact with the target material as the atomic number of the target material grows. Additionally, the likelihood of absorption within the target sample also escalates as the atomic number of the target material increases. Consequently, there comes a point where the rising atomic number of the target is adequate enough to offset a reduction in the quantity of multiple backscattered photons. Therefore, an observable increase in the number of multiple backscattered photons that emerge from the target becomes apparent.

Similar to the above, this study includes the calculation of data obtained by using the scattering values of radioactive rays on compounds with thermoluminescent properties. The radiation shielding properties of target materials are determined by calculating the scattering data ratio values, also called albedo factor parameters. This study aims to examine the capacities of materials frequently used in dosimeters to protect from radiation. In this direction, some radiation shielding parameters were calculated by evaluating the Compton and coherent peaks obtained from the scattering experiments. These calculations are presented in Figures 3, 4 and 5.

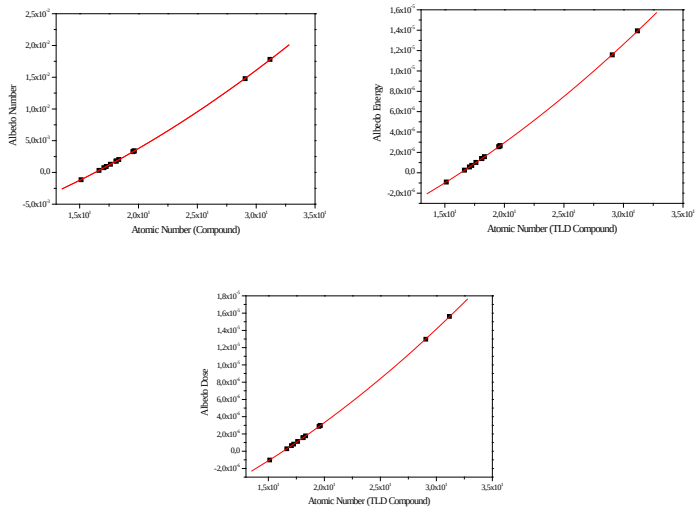


**Figure 3. Albedo Number versus atomic number (TLD Compound)**

**Figure 4. Albedo Energy versus atomic number (TLD Compound).**

**Figure 5. Albedo Dose versus atomic number (TLD Compound).**

As can be understood from the figures mentioned, the albedo values increase with the increase in atomic number. The reason for this situation is similar to the

results obtained in the studies conducted by many researchers before. In other words, it would be correct to say that backscattering increases with increasing atomic number, and in this case, the radiation-absorbing feature of the material examined decreases. The situation is no different for the thermoluminescent materials we examined in our study.

**Acknowledgments**

This work was supported by Şırnak University Research Fund (BAP): [Grant Number 2024.FNAP.06.02.02].

**REFERENCES**

[1] Ihsani, R. N., Gareso, P. L., & Tahir, D. (2024). An overview of gamma radiation shielding: Enhancements through polymer-lead (Pb) composite materials. *Radiation Physics and Chemistry*, 111619.

[2] Bakri, F., Gareso, P. L., & Tahir, D. (2024). Advancing radiation shielding: A review the role of Bismuth in X-ray protection. *Radiation Physics and Chemistry*, 111510.

[3] Chandrika, B. M., Manjunatha, H. C. S., Munirathnam, R., Sridhar, K. N., Seenappa, L., Manjunatha, S., ... & Gupta, P. D. (2024). Synthesis and characterization of BiBAl nanocomposite for radiation shielding. *Progress in Nuclear Energy*, *169*, 105061.

[4] Darwesh, R., Sayyed, M. I., Al-Hadeethi, Y., ALasali, H. J., & Alotaibi, J. S. (2024). Improved radiation shielding properties of epoxy resin composites using Sb2O3 and Al2O3 nanoparticles additives. *Annals of Nuclear Energy*, *200*, 110385.

[5] Biradar, S., Dinkar, A., Bennal, A. S., Devidas, G. B., Hareesh, B. T., Siri, M. K., ... & Chandrashekara, M. N. (2024). Comprehensive investigation of borate-based glasses doped with BaO: An assessment of physical, structural, thermal, optical, and radiation shielding properties. *Optical Materials*, *150*, 115176.

[6] Aldawood, S., Asemi, N. N., Kassim, H., Aziz, A. A., Saeed, W. S., & Al-Odayni, A. B. (2024). Gamma radiation shielding by titanium alloy reinforced by

polymeric composite materials. *Journal of Radiation Research and Applied Sciences*, *17*(1), 100793.

[7] Zakaria, M. A., Razab, M. K. A. A., Adenan, M. Z., Ahmad, M. Z., Tajudin, S. M., Samson, D. O., & Aziz, M. Z. A. (2024). Radiation attenuation and elemental composition of locally available ceramic tiles as potential radiation shielding materials for diagnostic X-ray rooms. *Nuclear Engineering and Technology*, *56*(1), 301-308.

[8] Akman, F., Khattari, Z. Y., Kaçal, M. R., Sayyed, M. I., & Afaneh, F. (2019). The radiation shielding features for some silicide, boride and oxide types ceramics. *Radiation Physics and Chemistry*, *160*, 9-14.

[9] Akman, F., Kaçal, M. R., Almousa, N., Sayyed, M. I., & Polat, H. (2020). Gamma-ray attenuation parameters for polymer composites reinforced with BaTiO3 and CaWO4 compounds. *Progress in nuclear energy*, *121*, 103257.

[10] Akman, F., Kaçal, M. R., Sayyed, M. I., & Karataş, H. A. (2019). Study of gamma radiation attenuation properties of some selected ternary alloys. *Journal of Alloys and Compounds*, *782*, 315-322.

[11] Turhan, M. F., Akman, F., Taşer, A., Dilsiz, K., Oğul, H., Kacal, M. R., & Agar, O. (2022). Gamma radiation shielding performance of CuxAg (1-x)-alloys: Experimental, theoretical and simulation results. *Progress in Nuclear Energy*, *143*, 104036.

[12] Turhan, M. F., Akman, F., Polat, H., Kaçal, M. R., & Demirkol, İ. (2020). Gamma-ray attenuation

behaviors of hematite doped polymer composites. *Progress in Nuclear Energy*, *129*, 103504.

[13] Uzunoğlu, Z., Yilmaz, D., & Şahin, Y. (2017). Determination of the saturation thickness and albedo factors for mercury (II) oxide and lead (II) oxide. *Instrumentation Science & Technology*, *45*(1), 111-121.

[14] Yılmaz, D., Uzunoğlu, Z., & Demir, C. (2017). Albedo factors of some elements in the atomic number range 26≤ Z≤ 79 for 59.54 keV. *Applied Radiation and Isotopes*, *122*, 68-71.

[15] Ljubenov, V. L., & Simović, R. D. (2013). Photon albedo coefficients as functions of μ/Zeff parameter. *Nuclear Technology and Radiation Protection*, *28*(3), 247-253.

[16] Akkuş, T. (2020). Determination of number, energy and dose albedos of samples with various mean atomic number for 59.54 keV gamma-rays. *Radiation Physics and Chemistry*, *170*, 108579.

[17] Akkuş, T., & Yılmaz, D. (2019). Dependence of albedo factors on mean atomic number for 662 keV gamma photons. *Applied Radiation and Isotopes*, *154*, 108870.

[18] Yılmaz, D., Uzunoğlu, Z., & Demir, C. (2017). Albedo factors of some elements in the atomic number range 26≤ Z≤ 79 for 59.54 keV. *Applied Radiation and Isotopes*, *122*, 68-71.

[19] Sabharwal, A. D., Singh, S., Singh, B., & Sandhu, B. S. (2011). Albedo factors of 279, 320, 511 and 662 keV

backscattered gamma photons. *Radiation Effects & Defects in Solids*, *166*(6), 451-458.

[20] Sabharwal, A. D., Singh, B., & Sandhu, B. S. (2009). Investigations of multiple backscattering and albedos of 1.12 MeV gamma photons in elements and alloys. *Nuclear Instruments and Methods in Physics Research Section B: Beam Interactions with Materials and Atoms*, *267*(1), 151-156.

[21] Kasap. S., Capper, P. Springer Handbook of Electronic and Photonic Materials,Springer Science+Business Media Inc., NewYork, USA, 2006, 1407.

[22] McKeever, S. W. S. Thermoluminescence of Solids, Cambridge University Press, Cambridge, England, 1985, 376.

# DYNAMIC CHARACTERISTICS OF MULTI-STEP, MULTI-CRACKED NON-UNIFORM BEAMS

**Mehmet HASKUL**[1]

**Murat KISA**[2]

## 1. INTRODUCTION

In buildings or industrial structures, stepped beams can be preferred according to different load carrying needs. In long-span bridges, stepped beams are used to increase the carrying capacity. Vibration analysis is a field of engineering study that examines the vibration behavior of a structure or system. This analysis aims to understand the effects of vibrations on structures or machines caused by external forces or internal dynamic loads. Vibration analysis often plays an important role in fields such as structural engineering, mechanical engineering, automotive engineering, and aerospace. The vibration problem of a cracked beam attracts the attention of many researchers. The presence of a crack in a beam will affect its dynamic properties, such as natural frequencies and mode shapes. Therefore, changes in the natural frequencies and mode shapes of the beam contain information about the

[1] Assoc. Prof. Dr., Şırnak University, Department of Mechanical Engineering, Faculty of Engineering, mehmethaskul@sirnak.edu.tr, ORCID: 0000-0001-8671-4597.

[2] Prof. Dr., Harran University, Department of Mechanical Engineering, Faculty of Engineering, mkisa@harran.edu.tr, ORCID: 0000-0001-7015-2198.

presence, location, and size of cracks. The main problem in investigating the vibration of a cracked beam is determining the local stiffness decrease at the crack location. In this section, a numerical method for free vibration analysis of a multi-step beam with multiple cracks was investigated.

Many studies on vibration analysis of beams, columns, and frame structures with uniform and variable cross-sections containing single or multiple cracks have been published in the literature (Salawu 1997; Dimarogonas 1996; Wauer 1990; Gasch 1993; Krawczuk and Ostachowicz 1996; Jassim et al. 2013; Kisa 2004; 2011; 2012; Kisa and Gurel 2006; 2007; Kisa et al. 1998; Kisa and Brandon 2000a; 2000b; Haskul and Kisa 2021a; 2021b; Aggumus and Guclu 2020; Turan and Aggumus 2021; Turan et al. 2024). There are also many studies in the literature examining the dynamic behavior of beams made of composite materials (Kisa and Gurel 2005; Kaya et al. 2018; Erdogan et al. 2023). Vibration analysis of stepped beams known in the literature was first discussed by Taleb and Suppiger (1961). In their work, the theory of integral equations applicable to the problem of free lateral vibration of beams and the Cauchy function method of the lowest frequency and modal configuration of a stepped beam were used. Sato (1980) used the transfer matrix approach to analyse nonlinear free vibrations of multi-step beams. El-Sayed and Farghaly (2017) provided an analytical, experimental, and three-dimensional finite element FE (3D) analysis approach for the modal analysis of stepped Timoshenko beams utilising the normalised transfer matrix method (NTM). Duan and Wang (2013) employed the

modified discrete singular convolution (DSC) approach for free vibration analysis of multi-step beams. Lu et al. (2009) developed a new approach for analyzing the free and forced vibrations of beams subjected to single or multi-step variations. Green's function was used in a method by Lee and Bergman (1994) to allow for both forced and free vibration of stepped linear beams or structures. Using first-order shear deformation beam theory and finite element formulation, Ju et al. (1994) investigated the effects of shear deformation and geometric parameters on the natural frequencies and mode shapes of beams with multistep cross-sections. Mao and Pietrzko (2010) and Mao (2011) examined the free vibrations of the stepped and multi-stepped Euler-Bernoulli beam using the Adomian decomposition method (ADM). Bambill et al. (2015) examined the free transverse vibrations of axially functionally graded stepped beams using the domain decomposition technique and the differential quadrature method, derived from the Timoshenko beam theory and the Hamilton principle method. Lee (2015) used the Chebyshev-tau method to analyze the free vibration of stepped Euler-Bernoulli and Timoshenko beams. Wang and Wang (2013) used the differential quadrature element method (DQEM) to analyze the free vibration problem of multi-step beams. Attar (2012) proposed an analytical approach to find the dynamic characteristics of a stepped beam containing multiple edge cracks. Su et al. (2018) proposed a formulation to analyze the modal analysis of multi-step Timoshenko beams with well-known boundary conditions. Vaz and Lima Junior (2016) investigated the natural frequencies and mode shapes of Euler-Bernoulli

stepped beams with elastic end supports. Šalinić et al. (2018) conducted vibration analysis of tapered, stepped and continuously section AFG bars and Euler-Bernoulli beams. Wattanasakulpong and Chaikittiratana (2016) applied the Adomian mode decomposition method to solve the large-amplitude vibration analysis of stepped beams with various general and elastic boundary conditions. Jaworski and Dowell (2008) theoretically examined the analysis of free vibration of a multi step cantilever beam and conducted an experimental study to verify the results they found. Cunedioglu and Shabani (2020) studied the free vibration analysis of multilayer symmetric sandwich shear Timoshenko beams with single-edge cracks made of functionally graded materials using the finite element method and linear elastic fracture mechanics theories. El Hantati et al. (2023) investigated the geometrically nonlinear forced vibration of mass-bearing multi-step beams based on Euler-Bernoulli beam theory and Von Karman's geometric non-linearity assumptions. Kim et al. (2022) proposed a solution using a Haar wavelet discretization method (HWDM) to analyze the free vibration of a multi-step functionally graded (FG) curved beam with general boundary conditions. Li and An (2023) presented analytical solutions of the natural frequencies and mode shapes of Euler-Bernoulli beams with step changes in stiffness. Alcheikh et al. (2021) presented the research on the dynamics of straight multi-step micro beams of micro-electro-mechanical systems (MEMS) by developing an analytical model based on Euler-Bernoulli beam theory and Galerkin discretization. Atcı (2024)

examined the nonlinear vibrations of cracked micro beams using modified couple stress theory.

## 2. MATHEMATICAL MODEL

The beam considered in this study is assumed to be an Euler-Bernoulli beam with variable cross-section and multiple cracks (see Fig. 1). In the finite element method, the beam is divided into n elements and each element has two nodes with three degrees of freedom at each node (see Fig. 2).

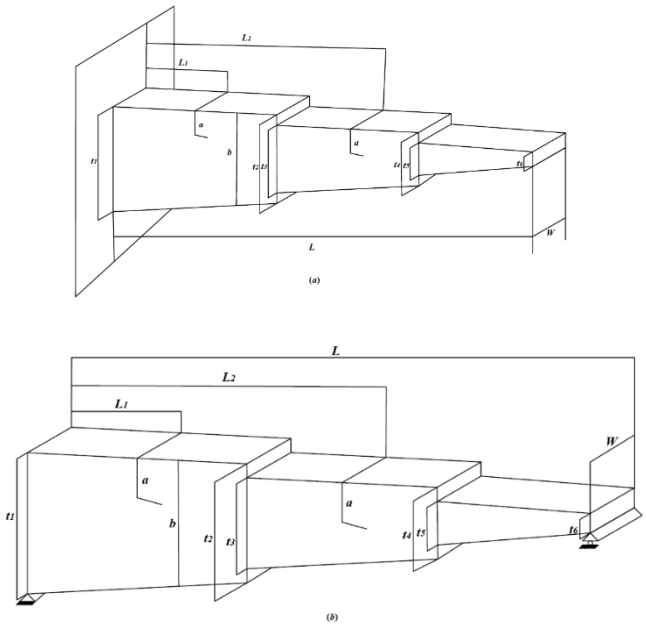


**Fig. 1. Multi-stepped tapered with multi-cracked beam (a) fixed-free ends and, (b) pinned-pinned ends**

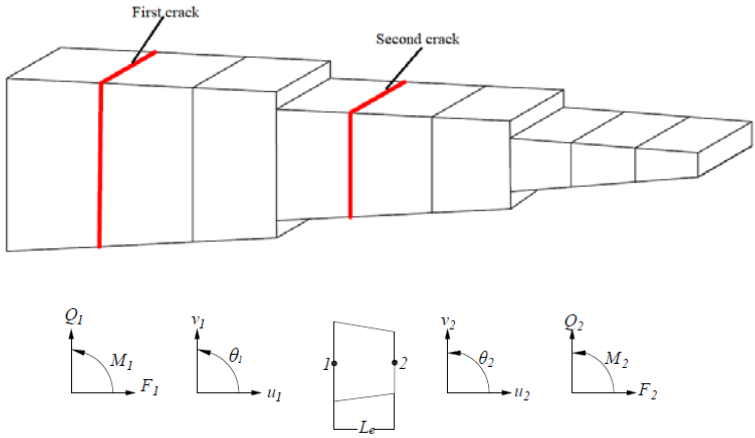


**Fig. 2. Finite element modelling of the multi-step tapered beam with multiple cracks**

### 2.1. Stiffness and mass matrices for the non-uniform beam

As shown in Fig. 2, the beam is divided into subcomponents, and each component has many elements and each element has two nodes with three degrees of freedom at each node. Accordingly, the stiffness matrix of an element, is given as follows:

$$[K_e] = [k_{ij}]_{6x6} \quad (1)$$

where $[K_e]$ element stiffness matrix and $k_{ij}$ $(i,j=1,\ldots,6)$ are obtained as follows. At a distance $x$ from the left end of the beam depicted in Fig. 1, the bending $EI_{zz}(x)$ and axial $EA(x)$ stiffnesses are as follows:

$$EI_{zz}(x) = EI_{zz1}\left(1 + \alpha\left(\frac{x}{L}\right)\right)^3 \quad (2)$$

$$EA(x) = EA_1\left(1 + \alpha\left(\frac{x}{L}\right)\right) \quad (3)$$

where $I_{zz1}$ and $A_1$ indicate the area moment of inertia and cross-sectional area of the left end, respectively. α for multi stepped beam is given as following:

$$\alpha = \frac{t_2 - t_1}{t_1} = \frac{t_4 - t_3}{t_3} = \frac{t_6 - t_5}{t_5} \tag{4}$$

where $t_i$ indicate the thicknesses of the non-uniform beam ($i$=1,..,6). The stiffness matrix of a non-uniform beam element can be calculated as follows:

$$[K_e] = \begin{bmatrix} \frac{1}{C} & 0 & 0 & -\frac{1}{C} & 0 & 0 \\ 0 & \frac{A_1}{D_1} & \frac{A_2}{D_1} & 0 & -\frac{A_1}{D_1} & \frac{A_1 L - A_2}{D_1} \\ 0 & \frac{A_2}{D_1} & \frac{A_3}{D_1} & 0 & -\frac{A_2}{D_1} & \frac{A_2 L - A_3}{D_1} \\ -\frac{1}{C} & 0 & 0 & \frac{1}{C} & 0 & 0 \\ 0 & -\frac{A_1}{D_1} & -\frac{A_2}{D_1} & 0 & \frac{A_1}{D_1} & \frac{A_2 - A_1 L}{D_1} \\ 0 & \frac{A_1 L - A_2}{D_1} & \frac{A_2 L - A_3}{D_1} & 0 & \frac{A_2 - A_1 L}{D_1} & \frac{A_1 L^2 - 2A_2 L + A_3}{D_1} \end{bmatrix} \tag{5}$$

where $A_1$, $A_2$, $A_3$, $D_1$ and $C$ are:

$$\left.\begin{aligned} A_i &= \int_0^L \frac{x^{(i-1)}}{EI_{zz}(x)}\,dx, \quad i = 1,2,3 \\ D_1 &= A_1 A_3 - A_2^2, \\ \frac{1}{C} &= \frac{EA_1}{L}\left[\frac{\alpha}{ln(\alpha+1)}\right] \end{aligned}\right\} \tag{6}$$

and the element mass matrix is,

$$[M_e] = \left[m_{ij}\right]_{6x6} \tag{7}$$

The mass matrix of a non-uniform beam element is given as follows:

$$[M_e] = \begin{bmatrix} m_{11}^A & 0 & 0 & m_{12}^A & 0 & 0 \\ 0 & m_{11}^B & m_{12}^B & 0 & m_{13}^B & m_{14}^B \\ 0 & m_{21}^B & m_{22}^B & 0 & m_{23}^B & m_{24}^B \\ m_{21}^A & 0 & 0 & m_{22}^A & 0 & 0 \\ 0 & m_{31}^B & m_{32}^B & 0 & m_{33}^B & m_{34}^B \\ 0 & m_{41}^B & m_{42}^B & 0 & m_{43}^B & m_{44}^B \end{bmatrix}_{6x6} \quad (8)$$

where $m^A{}_{ij}$ and $m^B{}_{ij}$ are:

$$[m]^A = \begin{bmatrix} \frac{1}{12}\rho A_1 L(4+\alpha) & \frac{1}{12}\rho A_1 L(2+\alpha) \\ \frac{1}{12}\rho A_1 L(2+\alpha) & \frac{1}{12}\rho A_1 L(4+3\alpha) \end{bmatrix} \quad (9)$$

$$[m]^B = \begin{bmatrix} \frac{1}{35}\rho A_1 L(13+3\alpha) & \frac{1}{420}\rho A_1 L^2(22+7\alpha) & \frac{9}{140}\rho A_1 L(2+\alpha) & -\frac{1}{420}\rho A_1 L^2(13+6\alpha) \\ & \frac{1}{840}\rho A_1 L^3(8+3\alpha) & \frac{1}{420}\rho A_1 L^2(13+7\alpha) & -\frac{1}{280}\rho A_1 L^3(2+\alpha) \\ & & \frac{1}{35}\rho A_1 L(13+10\alpha) & -\frac{1}{420}\rho A_1 L^2(22+15\alpha) \\ & Symmetric & & \frac{1}{840}\rho A_1 L^3(8+5\alpha) \end{bmatrix} \quad (10)$$

### 2.2.Compliance matrix of the crack

The fact that structures are constantly loaded, problems such as cracks can emerge. Cracks, for example, are local sources of flexibility that influence the dynamic and static behaviour of structures. The stress concentration factor helps predict the behaviour of cracks in damaged structures. Castigliano's theorem and stress intensity factors can be used to calculate the flexibility coefficients that occur within the structure as a result of cracks. The strain energy release rate *J* is the rate at which the strain energy of stress within the material changes across a crack. The strain energy release rate is critical for determining a material's cracking resistance and knowing how cracking will occur. For plane strain, *J* is given as (Tada *et al*. 1973).

$$J = \frac{1-v^2}{E} K_I^2 + \frac{1-v^2}{E} K_{II}^2 + \frac{1+v}{E} K_{III}^2 \quad (11)$$

where $E$ is the modulus of elasticity, $v$ is Poisson's ratio, and $K_I$, $K_{II}$ and $K_{III}$ are stress intensity factors for opening (mode *I*), sliding (mode *II*) and tearing (mode *III*) cracks. The relationship between the strain energy and the amount of strain energy release rate of a defective structure subjected to strain energy $U$, crack area $A$ and $P_i$ load is expressed as follows (Tada *et al*. 1973):

$$J = \frac{\partial U(P_i,A)}{\partial A} \quad (12)$$

According to Castigliano's theorem, the amount of additional displacement in the direction of the $P_i$ occurring due to the crack is as follows:

$$u_i = \frac{\partial U(P_i,A)}{\partial P_i} \quad (13)$$

By substituting Eq. (12) into Eq. (13), the final expression between displacement and strain energy release rate $J$ is found as follows:

$$u_i = \frac{\partial}{\partial P_i} \int_A J(P_i, A)\, dA \quad (14)$$

The flexibility coefficients can be given as:

$$c_{ij} = \frac{\partial u_i}{\partial P_j} = \frac{\partial^2}{\partial P_i \partial P_j} \int_A J(P_i, A)\, dA \quad (15)$$

Since it is known that the shear force does not affect the opening mode of the crack, the flexibility coefficients according to the δ ( $u$, $v$, $\theta$) displacement vector are written in matrix format as follows:

$$C = \begin{bmatrix} c_{11} & 0 & c_{13} \\ 0 & c_{22} & 0 \\ c_{31} & 0 & c_{33} \end{bmatrix} \quad (16)$$

The stiffness matrix for the crack is given below:

$$K_{cr} = \begin{bmatrix} [C]^{-1} & -[C]^{-1} \\ -[C]^{-1} & [C]^{-1} \end{bmatrix}_{6x6} \quad (17)$$

where $K_{cr}$ indicates the stiffness matrix occured due to cracks in the beam.

It is known that cracks within the structure cause a decrease in stifftness. (Irwin, 1960). Stiffness matrix of cracked beam, $[K]_{wcr}$ is given as:

$$[K]_{wcr} = [K] - [K]_{cr} \quad (18)$$

The free vibration equation is given below in matrix format:

$$[K]_{wcr} - \lambda[M]\varphi = 0 \quad (19)$$

Using Equation 19, the dynamic properties of a single and multi-stepped variable cross-section beam with a crack were obtained.

## 3. NUMERICAL RESULTS

Parameters of the beam are: $L$=0.18m; $t_1$=0.025m; and $W$ =0.0078m; modulus of elasticity E=216 GPa; Poisson ratio $v$=0.3 and density $\rho$=7850 kg/m$^3$ and the thickness ratio of the beam varies linearly ($t_2/t_1 = t_4/t_3 = t_6/t_5$). In this study, the natural frequencies and mode shapes of the cracked beam were examined for different ends of the multi-stepped non-uniform beam with multiple cracks.

### 3.1.Fixed-free ends

In this section; a free vibration analysis was performed on a fixed-free ends multi-stepped non-uniform beam with multiple cracks. Figs. 4, 5 and 6 show the first, second, and third non-dimensional natural frequencies of the fixed-free multi-stepped beam with multiple cracks for different taper ratios ($t_2/t_1$=0.75, 0.85, 0.95) and various of crack locations according to the crack depth ratios ($a/b$=0.2–0.8). In the Figs., the maximum decrease in the first natural frequencies occurred when the cracks were located close to the fixed ends, *Lc1/L=1/9* and *Lc2/L=2/9*. The second and third natural frequencies showed maximum decreases when the cracks were at *Lc1/L=1/9*, *Lc2/L=5/9*, and *Lc1/L=4/9*, *Lc2/L=7/9*, respectively. These frequency drops in the cracked beam can be expressed as an indicator of significant energy losses resulting from cracks located in sections with high bending moments.

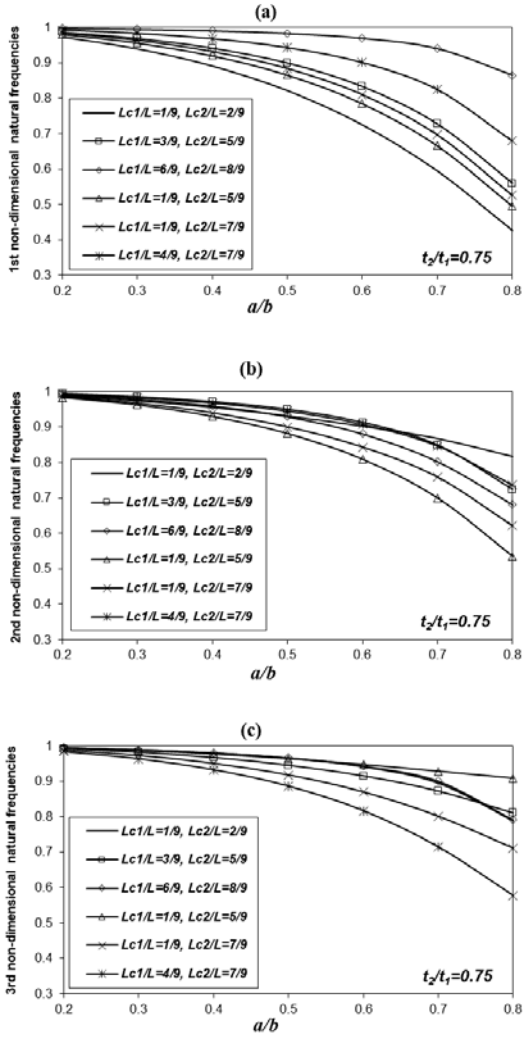


**Fig. 4. (a) First (b) Second (c) Third, non-dimensional natural frequencies for taper ratio $t_2/t_1$=0.75**

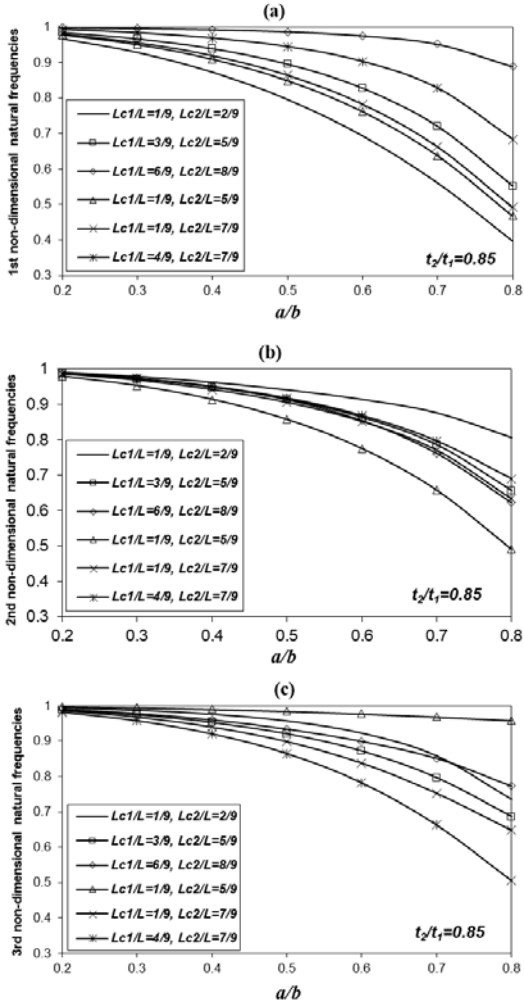


**Fig. 5. (a) First (b) Second (c) Third, non-dimensional natural frequencies for taper ratio $t_2/t_1$=0.85**

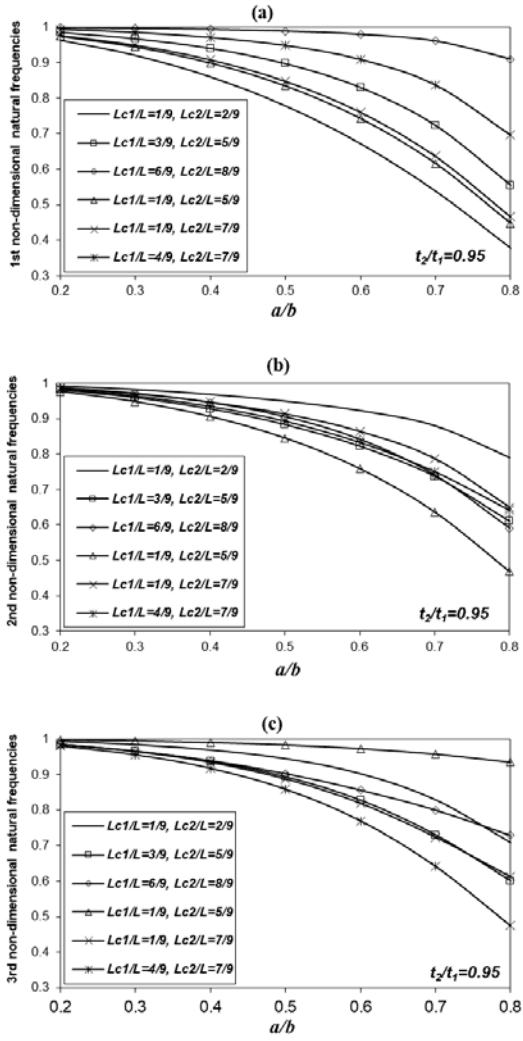


**Fig. 6. (a) First (b) Second (c) Third, non-dimensional natural frequencies for taper ratio $t_2/t_1$=0.95**

Fig. 7 show the first, second and third mode shapes variations depending on the crack locations for the different taper ratios and the crack depth ratio *a/b=0.8*. Mode shapes show the displacements of the beam during vibration. As can be seen from the oscillatory movements of mode shapes, vibration becomes more effective as the

thickness decreases. It also reveals the effect of crack locations and crack depth ratio.

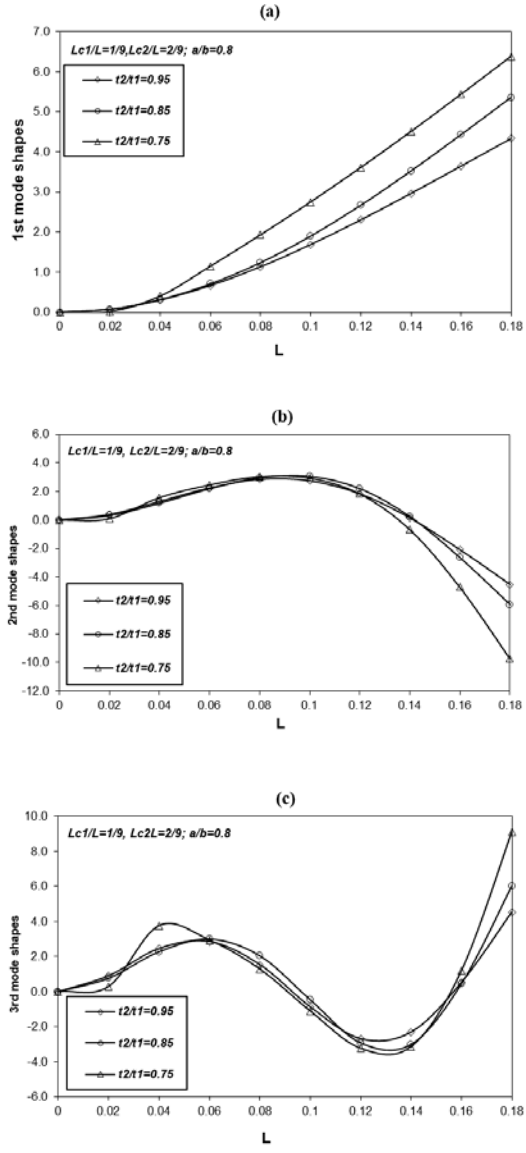


**Fig. 7. (a) First, (b) Second, (c) Third, mode shapes of fixed-free multi-stepped beam with multiple cracks for crack depth ratio *a/b*=0.8 and different taper ratios**

### 3.2.Pinned-pinned ends

In this section; a free vibration analysis was performed on a pinned-pinned multi-stepped beam with tapered cross-section and multiple cracks. Figs. 8, 9, and 10 show the first, second, and third non-dimensional natural frequencies of the pinned-pinned ends multi-stepped beam with different taper ratios ($t_2/t_1$ =0.75, 0.85, 0.95) and the various multiple crack locations depending on crack depth ratios ($a/b$=0.2–0.8). In the Figs., when the location of the cracks were at $Lc1/L$=4/9, $Lc2/L$=7/9 for taper ratio $t_2/t_1$ =0.75 and $Lc1/L$=3/9, $Lc2/L$=5/9 for taper raitos $t_2/t_1$ =0.85, 0.95 the first natural frequencies decreased to its maximum. The reason for this is that the maximum moment in the pinned-pinned beam occurs at the midpoint and cracks close to these points cause more moment losses and lead to high energy drops. It can be seen from the figures that the change in the taper ratios of the beam also affects the change in natural frequencies.

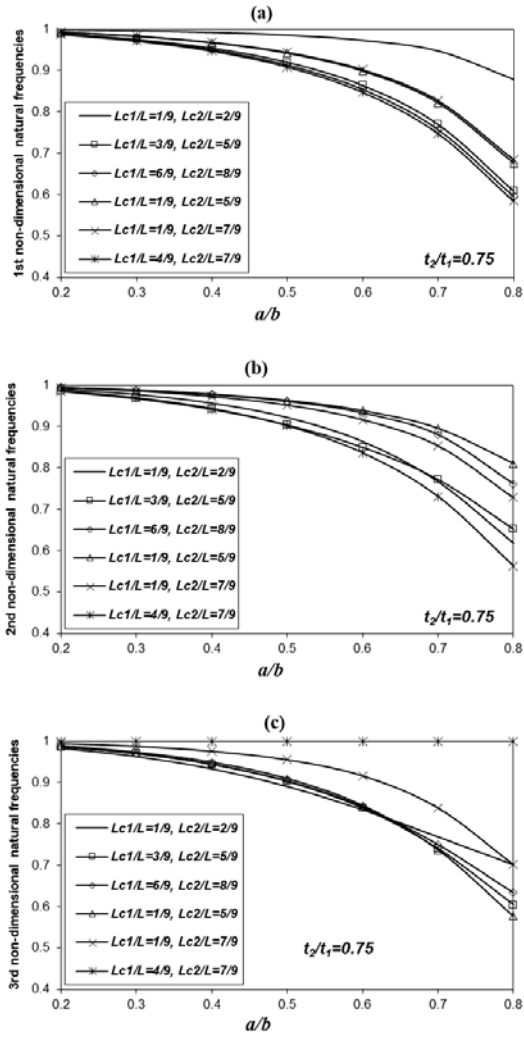


**Fig. 8. (a) First (b) Second (c) Third, non-dimensional natural frequencies for taper ratio $t_2/t_1$=0.75**

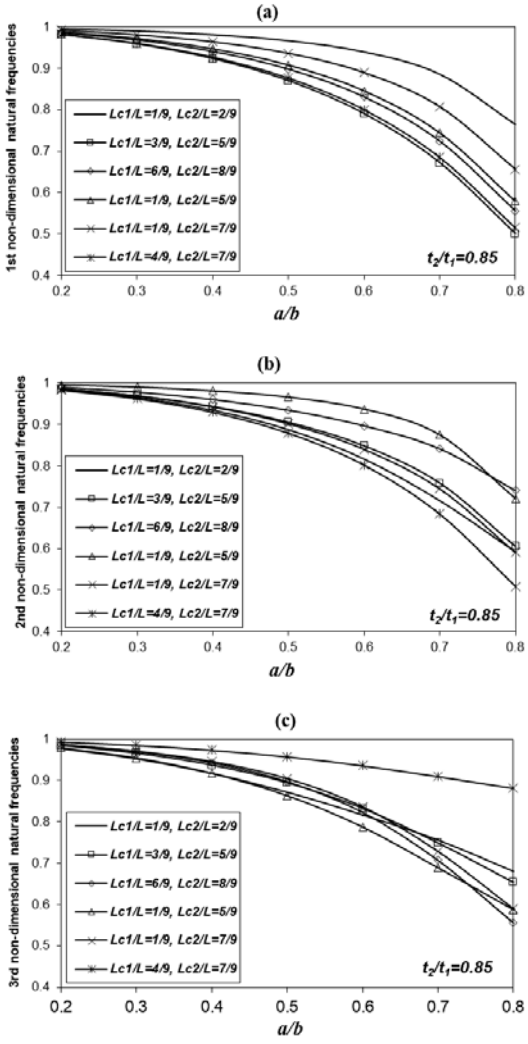


**Fig. 9. (a) First (b) Second (c) Third, non-dimensional natural frequencies for taper ratio $t_2/t_1$=0.85**

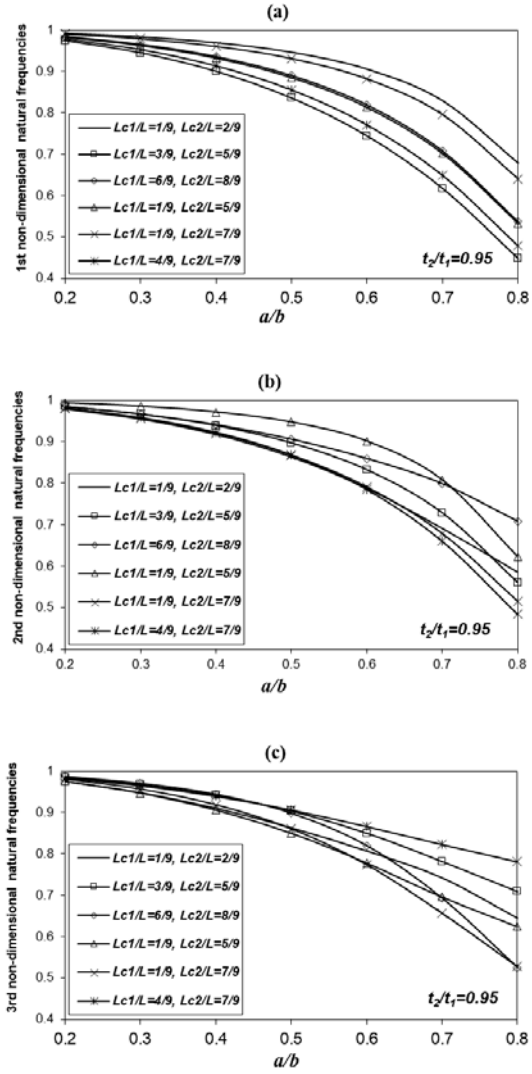


**Fig. 10. (a) First (b) Second (c) Third, non-dimensional natural frequencies for taper ratio $t_2/t_1$=0.95**

Fig. 11 shows the first, second and third mode shapes variations depending on multiple crack locations for the different taper ratios ($t_2/t_1$=0.75, 0.85, 0.95) and the crack depth ratio $a/b$=0.8. The figures clearly show how mode shapes are affected by the location of cracks. Larger

energy losses and significant changes in the relevant mode shapes will result from cracks located in the vicinity of the relevant mode's maximum bending moment regions.

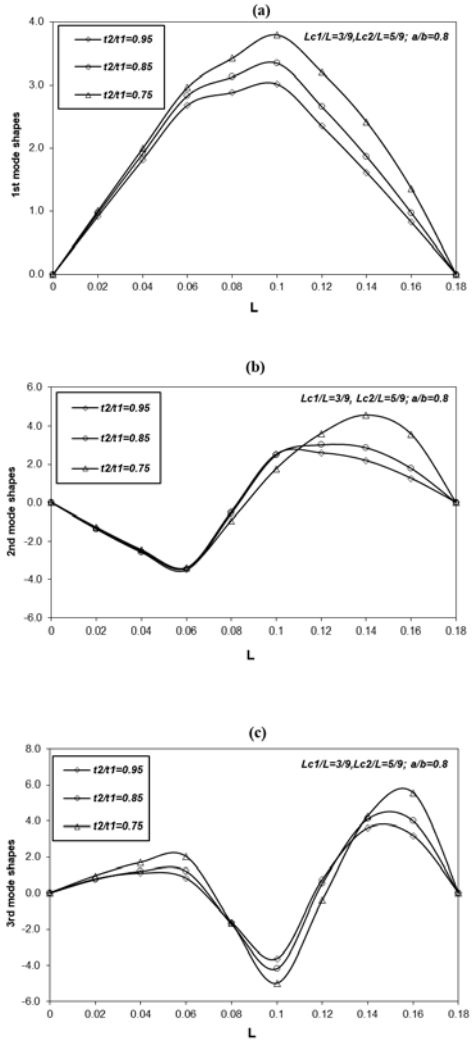


**Fig. 11. (a) First, (b) Second, (c) Third, mode shapes of fixed-free multi-stepped beam with multiple cracks for crack depth ratio *a/b*=0.8 and different taper ratio**

## 4. CONCLUSION

In this study, a free vibration analysis of a multi-step, nonuniform beam with multiple cracks and different ends was performed. Finite element method and component mode synthesis methods were used in the study. The crack in the beam gives local flexibility to the beam and the cracks are modeled as massless spring. Spring stiffness was obtained using the principles of linear fracture mechanics. System matrices such as stiffness and mass matrices, as well as stiffness matrices resulting from cracks, were calculated and free vibration analysis of the beam was carried out with the method given in this study. A computer program was prepared to calculate the natural frequencies and mode shapes of the beam, and in the program, natural frequencies and mode shapes were obtained according to crack locations, depth ratios and taper ratios, and the results were shown graphically.

In this study, cracks are taken into account as edge and open crack models. The results of the study were obtained for fixed-free and pinned-pinned-ends non-uniform beams. It is clearly seen in the figures that the changes in natural frequencies in the fixed free-end beam decrease more when the crack locations are close to the fixed end. On the other hand, it has been observed that when the cracks in the pinned-pinned-end non-uniform beam are close to the middle part of the beam, the changes in natural frequencies are reduced more. In addition, it has been observed that there are large changes in mode shapes near crack sections in parallel with the natural frequency changes near crack locations, and in this sense, it is of great

importance to check all mode shapes for crack detection. This result is important for damage detection through mode shapes. These changes in natural frequencies and mode shapes provide us important information about the depth and location of the crack in the beam.

The magnitude of energy loss caused by cracks depend on their sizes and locations. The bending moment in the beam section varies with the boundary and loading conditions along the beam. A crack in a section of the beam where the bending moment is greatest will result in significant energy loss and will also affect the beam's dynamic behavior. This study clearly demonstrated all of these findings.

**REFERENCES**

Aggumus, H., & Guclu, R. (2020, July). Robust H∞ control of STMDs used in structural systems by hardware in the loop simulation method. *In Actuators* (Vol. 9, No. 3, p. 55). MDPI.

Aggumus, H., Daskin, M., Haskul, M., & Turan, A. (2024). The Effect of the Crack-Stiffness Relationship on the System Response in Columns of an SDOF Steel Structure Model under Harmonic and Earthquake Excitations. *Shock and Vibration*, 2024(1), 9278849.

Alcheikh, N., Ouakad, H. M., & Younis, M. I. (2021). Dynamic analysis of straight stepped microbeams. *International Journal of Non-Linear Mechanics*, *128*, 103639.

Atcı, D. (2024). Nonlinear vibrations of cracked microbeams based on modified couple stress theory. *European Journal of Mechanics-A/Solids*, *106*, 105321.

Attar, M. (2012). A transfer matrix method for free vibration analysis and crack identification of stepped beams with multiple edge cracks and different boundary conditions. *International Journal of Mechanical Sciences*, *57*(1), 19-33.

Bambill, D. V., Rossit, C. A., & Felix, D. H. (2015). Free vibrations of stepped axially functionally graded Timoshenko beams. *Meccanica*, *50*, 1073-1087.

Cunedioglu, Y., & Shabani, S. (2020). Free vibration analysis of a single edge cracked symmetric functionally

graded stepped beams. *Advances in Structural Engineering*, *23*(16), 3415-3428.

Dimarogonas, A. D. (1996). Vibration of cracked structures: a state of the art review. *Engineering fracture mechanics*, 55(5), 831-857.

Duan, G., & Wang, X. (2013). Free vibration analysis of multiple-stepped beams by the discrete singular convolution. *Applied Mathematics and Computation*, *219*(24), 11096-11109.

El Hantati, I., Adri, A., El Khouddar, Y., Fakhreddine, H., Outassafte, O., & Benamar, R. (2023). Large amplitude forced vibrations of multi-stepped beams carrying concentric masses. *Mechanics Research Communications*, *132*, 104163.

El-Sayed, T. A., & Farghaly, S. H. (2017). A normalized transfer matrix method for the free vibration of stepped beams: comparison with experimental and FE (3D) methods. *Shock and Vibration*, *2017*(1), 8186976.

Erdoğan, İ., Kısa, M., Özen, M., Demircan, G., & Kaya, A. İ. Investigation of Dynamic Behavior of Glass Fiber Reinforced Epoxy Nanocomposites. Harran University Journal of Engineering, 8(2), 78-90.

Gasch, R. (1993). A survey of the dynamic behaviour of a simple rotating shaft with a transverse crack. *Journal of sound and vibration*, 160(2), 313-332.

Haskul, M., & Kisa, M. (2021). Free vibration of the double tapered cracked beam. *Inverse Problems in Science and Engineering*, 29(11), 1537-1564.

Haskul, M., & Kisa, M. (2021). Free-vibration analysis of cracked beam with constant width and linearly varying thickness. *Emerging Materials Research*, 11(1), 125-137.

Irwın, G. (1960). Fracture Mechanics, Editors JN Goodier and NJ Hoff.

Jassim, Z. A., Ali, N. N., Mustapha, F., & Jalil, N. A. (2013). A review on the vibration analysis for a damage occurrence of a cantilever beam. *Engineering Failure Analysis*, 31, 442-461.

Jaworski, J. W., & Dowell, E. H. (2008). Free vibration of a cantilevered beam with multiple steps: Comparison of several theoretical methods with experiment. *Journal of sound and vibration*, *312*(4-5), 713-725.

Ju, F., Lee, H. P., & Lee, K. H. (1994). On the free vibration of stepped beams. *International journal of solids and structures*, *31*(22), 3125-3137.

Kaya, A. I., Kisa, M., & Ozen, M. (2018). Influence of natural weathering conditions on the natural frequency change of woven carbonfibre reinforced composites. Advanced Composites Letters, 27(2), 096369351802700201.

Kim, K., Kwak, S., Jang, P., Juhyok, U., & Pang, K. (2022). Free vibration analysis of a multi-stepped functionally graded curved beam with general boundary conditions. *Proceedings of the Institution of Mechanical Engineers, Part C: Journal of Mechanical Engineering Science*, *236*(11), 5916-5939.

Kisa, M. (2004). Free vibration analysis of a cantilever composite beam with multiple cracks. *Composites Science and Technology*, 64(9), 1391-1402.

Kisa, M. (2011). Vibration and stability of multi-cracked beams under compressive axial loading. *International Journal of the Physical Sciences*, 6(11), 2681-2696.

Kisa, M. (2012). Vibration and stability of axially loaded cracked beams. *Structural engineering and mechanics*: *An international journal*, 44(3), 305-323.

Kisa, M., & Arif Gurel, M. (2005). Modal analysis of cracked cantilever composite beams. Structural Engineering and Mechanics, 20(2), 143-160.

Kisa, M., & Brandon, J. (2000). The effects of closure of cracks on the dynamics of a cracked cantilever beam. *Journal of sound and vibration*, 238(1), 1-18.

Kisa, M., & Brandon, J. A. (2000). Free vibration analysis of multiple open-edge cracked beams by component mode synthesis. Structural engineering and mechanics: *An international journal*, 10(1), 81-92.

Kisa, M., & Gurel, M. A. (2006). Modal analysis of multi-cracked beams with circular cross section. *Engineering Fracture Mechanics*, 73(8), 963-977.

Kisa, M., & Gurel, M. A. (2007). Free vibration analysis of uniform and stepped cracked beams with circular cross sections. *International Journal of Engineering Science*, 45(2-8), 364-380.

Kisa, M., Brandon, J., & Topçu, M. (1998). Free vibration analysis of cracked beams by a combination of finite elements and component mode synthesis methods. *Computers & structures*, 67(4), 215-223.

Krawczuk, M., & Ostachowicz, W. (1996). Damage indicators for diagnostic of fatigue cracks in structures by vibration measurements–a survey. *Journal of Theoretical and Applied Mechanics*, 34(2), 307-326.

Lee, J. (2015). Application of Chebyshev-tau method to the free vibration analysis of stepped beams. *International Journal of Mechanical Sciences*, *101*, 411-420.

Lee, J., and Bergman, L. A. (1994). The vibration of stepped beams and rectangular plates by an elemental dynamic flexibility method. *Journal of Sound and Vibration*, 171(5), 617-640.

Li, L., & An, S. (2023). Analytical solution and free vibration analysis for beams with step changes in stiffness. *Multidiscipline Modeling in Materials and Structures*, *19*(5), 1042-1054.

Lu, Z. R., Huang, M., Liu, J. K., Chen, W. H., & Liao, W. Y. (2009). Vibration analysis of multiple-stepped beams with the composite element model. *Journal of Sound and Vibration*, *322*(4-5), 1070-1080.

Mao, Q. (2011). Free vibration analysis of multiple-stepped beams by using Adomian decomposition method. *Mathematical and computer modelling*, *54*(1-2), 756-764.

Mao, Q., & Pietrzko, S. (2010). Free vibration analysis of stepped beams by using Adomian decomposition method. *Applied Mathematics and computation*, *217*(7), 3429-3441.

Salawu, O. S. (1997). Detection of structural damage through changes in frequency: a review. *Engineering structures*, 19(9), 718-723.

Šalinić, S., Obradović, A., & Tomović, A. (2018). Free vibration analysis of axially functionally graded tapered, stepped, and continuously segmented rods and beams. *Composites Part B: Engineering*, *150*, 135-143.

Sato, H. (1980). Non-linear free vibrations of stepped thickness beams. *Journal of Sound and Vibration*, *72*(3), 415-422.

Su, Z., Jin, G., & Ye, T. (2018). Vibration analysis of multiple-stepped functionally graded beams with general boundary conditions. *Composite Structures*, *186*, 315-323.

Tada, H., Paris, P. C., and Irwin, G. R. (1973). *The stress analysis of cracks*. Handbook, Del Research Corporation.

Taleb, N. J., & Suppiger, E. W. (1961). Vibration of stepped beams. *Journal of the Aerospace Sciences*, *28*(4), 295-298.

Turan, A., & Aggümüş, H. (2021). Implementation of advanced PID control algorithm for SDOF system. *Journal of Soft Computing and Artificial Intelligence*, *2*(2), 98-107.

Turan, A., Aggümüş, H., & Daşkın, M. (2024). PI-PD Controller Design Based on Weighted Geometric Center Method for Time Delay Active Suspension Systems. *Black Sea Journal of Engineering and Science*, 7(1), 89-95.

Vaz, J. D. C., & de Lima Junior, J. J. (2016). Vibration analysis of Euler-Bernoulli beams in multiple steps and different shapes of cross section. *Journal of Vibration and Control*, *22*(1), 193-204.

Wang, X., & Wang, Y. (2013). Free vibration analysis of multiple-stepped beams by the differential quadrature element method. *Applied Mathematics and Computation*, *219*(11), 5802-5810.

Wattanasakulpong, N., & Chaikittiratana, A. (2016). Adomian-modified decomposition method for large-amplitude vibration analysis of stepped beams with elastic boundary conditions. *Mechanics Based Design of Structures and Machines*, *44*(3), 270-282.

Wauer, J. R. (1990). On the dynamics of cracked rotors: a literature survey. *Applied Mechanics Reviews* 43 (1) 13–17.

# SCIENTIFIC RESEARCH AND EVALUATIONS 2024

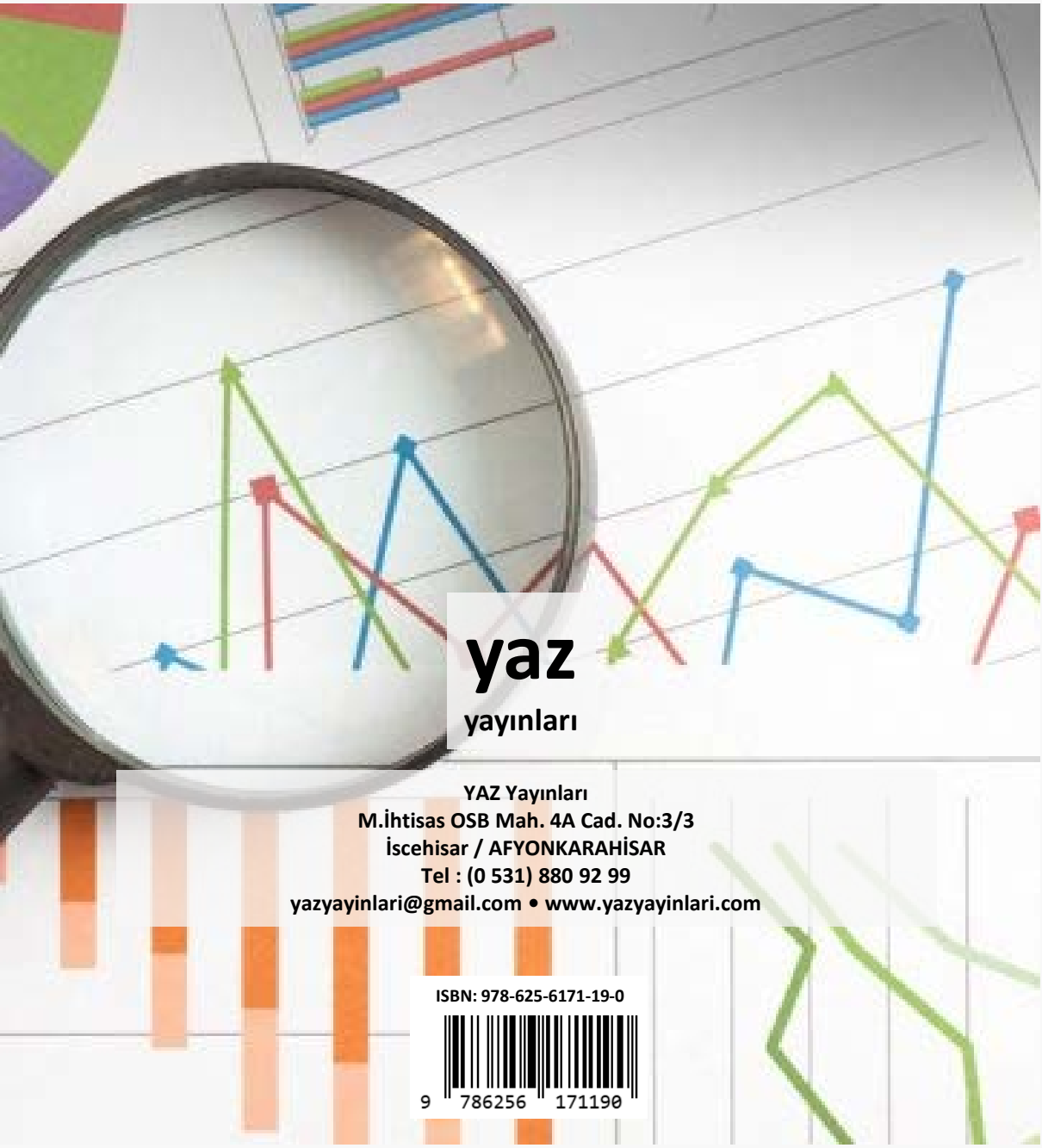

yaz
yayınları

YAZ Yayınları
M.İhtisas OSB Mah. 4A Cad. No:3/3
İscehisar / AFYONKARAHİSAR
Tel : (0 531) 880 92 99
yazyayinlari@gmail.com • www.yazyayinlari.com

ISBN: 978-625-6171-19-0